

Ludwig-Maximilians-Universität München

Sektion Physik

**Search for the Standard Model Higgs Boson  
in  $e^+e^-$  Collision at  $\sqrt{s} \approx 189$  GeV.  
at the OPAL experiment.**

A Diplomarbeit by

**Ane Terpger Rasmussen**

November 1999

**Erstgutacher: Prof. Dr. D. Schaile**

**Zweitgutachter: Prof. Dr. W.Dünnweber**

**Vejleder: Bent Ch. Jørgensen, Roskilde Universitetscenter**

# Contents

<b>1</b>	<b>Introduction</b>	<b>3</b>
<b>2</b>	<b>The OPAL experiment</b>	<b>5</b>
2.1	The tracking detectors . . . . .	8
2.1.1	The drift chambers . . . . .	8
2.2	The Time-Of-Flight detector . . . . .	10
2.3	The calorimeters . . . . .	10
2.4	Muon chamber and forward detector . . . . .	11
<b>3</b>	<b>The Electroweak Standard Model</b>	<b>13</b>
3.1	Elementary particles . . . . .	13
3.2	The Higgs bosons in the Standard Model . . . . .	15
3.2.1	The Higgs mechanism . . . . .	15
3.2.2	The Standard Model Higgs decay . . . . .	17
<b>4</b>	<b>The Analysis</b>	<b>19</b>
4.1	Selection of events . . . . .	19
4.1.1	The jet finder . . . . .	19
4.2	Likelihood classification of events . . . . .	22
4.2.1	Likelihood input variables . . . . .	24
4.3	The kinematic variable $P_k$ . . . . .	24
4.3.1	Constrained fit procedure . . . . .	24
4.3.2	Convergence . . . . .	26
4.3.3	Derivatives . . . . .	26
4.3.4	$\chi^2$ probability . . . . .	26
4.3.5	Weights estimate . . . . .	26
4.3.6	The weights parameterisation . . . . .	28
4.3.7	Kinematic fit of the event . . . . .	29
4.4	The b-tagging variable $P_b$ . . . . .	29
4.4.1	Secondary vertex . . . . .	29
4.4.2	Semi-leptonic decay . . . . .	31
4.4.3	The b-tagging probability . . . . .	31
4.5	The thrust variable $P_t$ . . . . .	31
4.6	The stability of the event as a 4 jet event $P_y$ . . . . .	31
<b>5</b>	<b>Discussion</b>	<b>35</b>
5.1	The likelihood distribution . . . . .	35
5.2	Efficiency and purity . . . . .	36
5.3	The recoiling mass . . . . .	37

**A Additional plots**

**39**

**Bibliography**

**45**



# Chapter 1

## Introduction

The only particle in the Electroweak Standard Model that has not yet been found is the Higgs boson. The Higgs boson search is therefore very interesting and the discovery of the boson would confirm the Electroweak Standard Model. If the Higgs boson is not found it would indicate that the Electroweak Standard Model is not sufficient to describe the elementary particles and their interactions. There are already different existing theories that go beyond the Electroweak Standard Model, among the most well known are the Minimal Super Symmetric Standard Model (MSSM) which is a particular case of the more general Super Symmetry (SUSY) theory.

In the Electroweak Standard Model masses are generated through spontaneous symmetry breaking where a scalar boson, the Higgs boson, occurs. The spontaneous symmetry breaking is also referred to as the Higgs mechanism, described by P.W. Higgs in 1964.

The presented work describes a search for the neutral Higgs boson performed with data taken at the Large Electron Positron collider (LEP) at a centre-of-mass energy of 189 GeV. The analysis is based on data collected in the summer and autumn of 1998 at the OPAL experiment. The OPAL experiment is one of the four experiments at the LEP collider at CERN the European Laboratory for Particle Physics.

In this analysis we describe a general method that is sensitive to any heavy boson decaying to  $b\bar{b}$  recoiling against a  $Z^0$  boson and produced together with the  $Z^0$  boson. The most interesting example within the framework of the Electroweak Standard Model is  $e^+e^- \rightarrow HZ^0$ . At this centre-of-mass energy the Higgs boson will predominately be produced via Higgsstrahlung, where the Higgs boson is produced in addition to a  $Z^0$  boson. The analysis concerns the channel where both the Higgs boson  $H$  and the  $Z^0$  boson decay into two quarks. This is commonly referred to as the 4-jet channel. The kinematic limit in this analysis for the Higgs bosons mass produced via Higgsstrahlung is  $M_H < 189 \text{ GeV} - 91 \text{ GeV} = 98 \text{ GeV}$ . The lower limit on the mass of the Higgs boson is  $> 89.7 \text{ GeV}/c^2$  that is taken from the LEP combined paper from April, 1999 [1]. Within this mass range the Higgs boson is expected to decay to  $b\bar{b}$  with a branching ratio of over 80%.

The aim of the work is to make optimisation studies of the selection criteria for the Higgs boson signal in the 4-jet channel. The errors on the measured jets energy and momenta are then studied as a function of a selected set of event kinematic and topology variables. An iterative procedure is used for a constrained kinematic fit. This procedure, that uses as input the jet measured quantities and their associated errors, is tuned to produce a single output variable that discriminates between the searched signal and the main background sources. To further separate the Higgs signal from background a likelihood is constructed out of 4 variables: the kinematic fit output, a b jet tagging probability and two other variables related to the general event shape namely the event thrust and the jet finder resolution parameter. The signal selection efficiency and purity are studied as a

function of the likelihood. A cut on the likelihood leads to a selection of events from data. The amount of selected events and their di-jet mass distribution is compared to the sample of expected background and signal events (for a given Higgs mass) after which a mass limit is derived for the Higgs bosons mass  $M_H$ .

This report begins with a brief description of the OPAL detector, followed by a short review of the Electroweak Standard Model. The analysis is then described and results are presented.

## Chapter 2

# The OPAL experiment

The Omni-Purpose Apparatus at LEP<sup>1</sup>, referred to as the OPAL detector is designed to identify and measure the kinematic of particles produced in  $e^+e^-$  collisions with centre-of-mass energies up to 200 GeV. OPAL is one of four LEP experiments at CERN<sup>2</sup>, the European Laboratory for Particle Physics. In the first phase (1989 to 1995) LEP was running with centre-of-mass energies around the  $Z^0$  mass. At the end of the first phase more than 10 million  $Z^0$  decays were collected by the 4 LEP experiments together, and important achievements on precision measurements of the  $Z^0$  line-shape and electro-weak parameters were obtained. For the second phase (since 1995) LEP started with centre-of-mass energies close to the  $W^-W^+$  pair production threshold (133 GeV) in 1995. The centre-of-mass energies was then gradually increased to reach 202 GeV for part of the 1999 run. During this phase, the electro-weak measurements were complemented by the studies of the  $W^+W^-$  pair production. The search for the standard model Higgs as well as signatures for new physics were performed at each new LEP centre-of-mass energy.

The OPAL detector consists of several layers of different sub-detectors, each with a different purpose and design. OPAL has a cylindrical shape and it is divided into a “barrel” region at the centre, and “endcaps” at either end. The OPAL detector covers nearly the whole  $4\pi$  solid angle. Often the collected information from a single sub-detector is not sufficient to provide unambiguous particle measurements. Instead information from the several sub-detectors must be combined. A drawing of the OPAL detector is shown in figure 2.1.

For the best reconstruction of the events, it is preferable to have equal detector capabilities in both the barrel and the endcap regions. However, this is not entirely possible due to the beam pipe in the endcaps. Furthermore there are detectors unique to the endcaps used to measure the luminosity. The different sub-detectors relevant to this analysis will be briefly described. A detailed description of the OPAL detector is given in [2].

In figure 2.2 a cross-section of the detector can be seen; the upper part of figure 2.2 (part a) shows the barrel component of the detector seen from the endcap. The lower part of the figure (part b) shows the endcap seen from above. As shown in figure 2.1, the OPAL reference frame is defined such the beam direction is parallel to the z-axis. The positive z direction is along the electron beam and the x-axis points to the centre of the LEP ring. The polar angle  $\theta$  is defined with respect to the positive z direction, the azimuthal angle  $\phi$  with respect to the positive x direction. The two beams come from each side and are set to collide in the middle of the detector at the interaction point also called the vertex.

---

<sup>1</sup>The Large Electron Positron collider

<sup>2</sup>CERN: Conseil Européen pour la Recherche Nucléaire



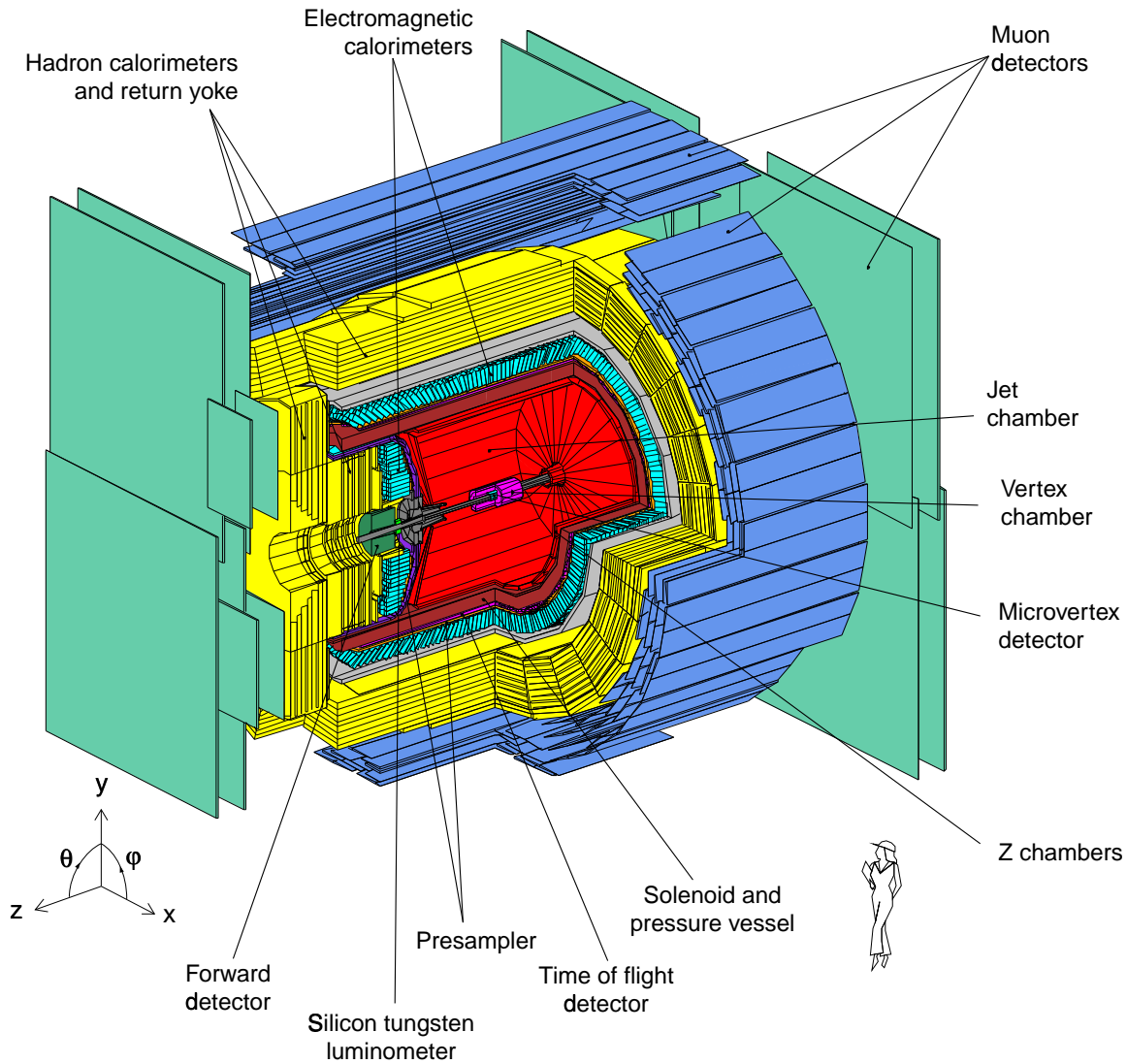


Figure 2.1: The OPAL detector.

In principle only stable particles like  $e^\pm$ 's,  $\mu^\pm$ 's and  $\gamma$ 's are directly measured. Non stable or very short lived particles like  $\tau$ 's, b mesons and  $\pi^0$ 's are reconstructed by the measurement of their decay products.

The OPAL sub-detectors can be divided into 2 major groups, the tracking detectors and the calorimeters. Table 2.1 shows in which detector group the different particles give a signal (x) and deposit all or a significant fraction of their their energy (X).

The tracking chambers are located in a 0.435 Tesla magnetic field created by the solenoid, see figure 2.2. The particles momentum and charge are derived from the curvature of the particles trajectory in the magnetic field. The particle energy is measured by the the calorimeters that consist of an electro-magnetic part and a hadronic part.

Part of the fast information from sub-detectors is used to build the OPAL triggering logic. The rest of the sub-detectors information is read out whenever one or more good trigger conditions are met. The OPAL trigger efficiency is nearly 100% for most of the important physics processes.

Specific sub-detectors located in the forward regions close to the beam pipe, were designed to

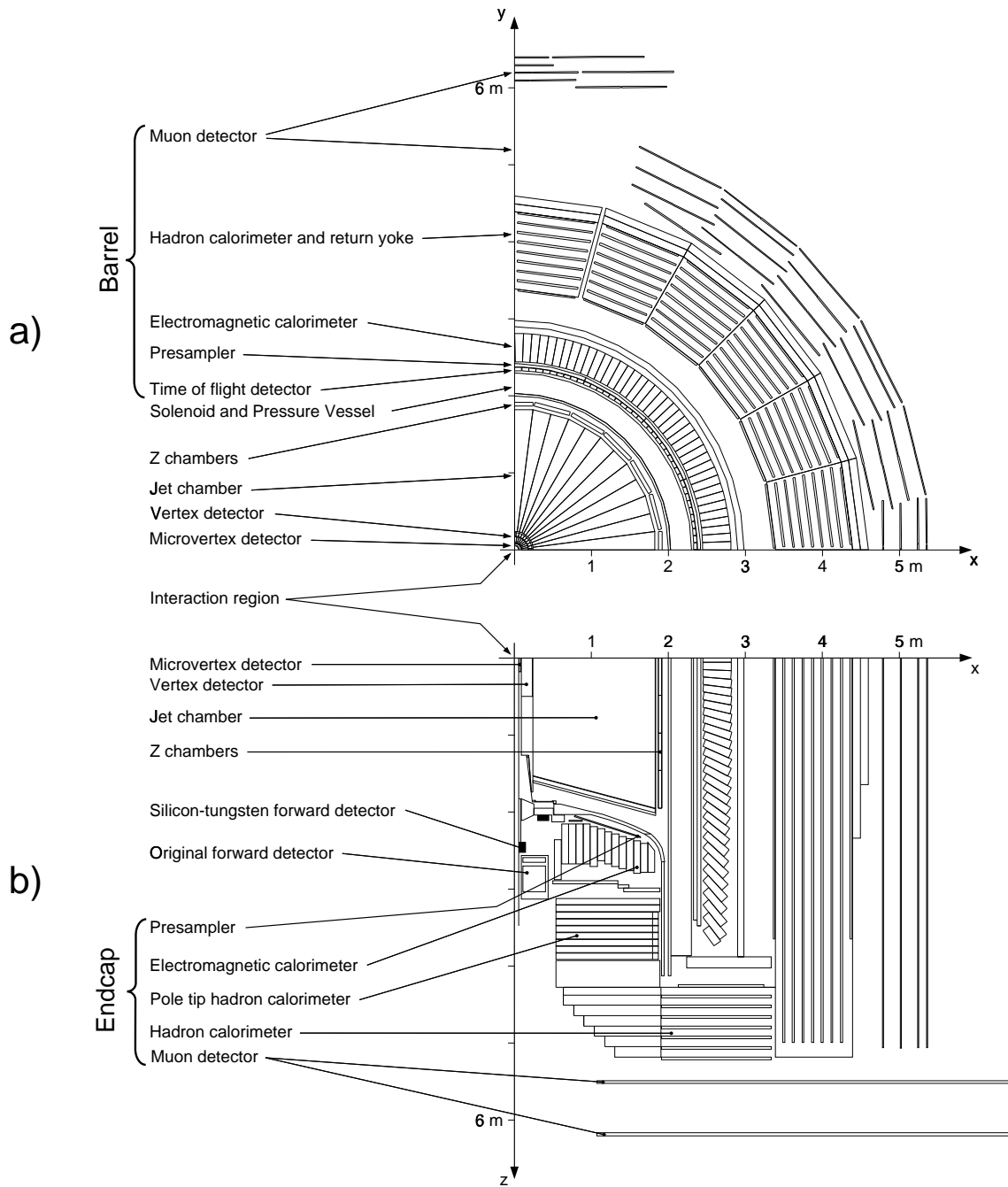


Figure 2.2: Cross-section of the OPAL detector. a: perpendicular to the beam pipe and b: parallel to the beam pipe.

measure the luminosity. The luminosity is estimated from the measured rate of low angle Bhabha ( $e^+e^- \rightarrow \gamma \rightarrow e^+e^-$ ) scattering. A precise integrated luminosity evaluation is required for all the studies that need an absolute cross section measurement.

Muon Chamber					x	
Hadron Calorimeter			X	X	x	
Electromagnetic Cal.	X	X	x	x	x	
Scintillators	x	x		x	x	
Tracking detectors	x			x	x	
Particles	$e^\pm$	$\gamma$	n	$p^\pm$ , hadrons $^\pm$	$\mu$	$\nu$

Table 2.1: Different particle signals in the detectors.

## 2.1 The tracking detectors

The OPAL tracking system consists of a set of complementary tracking detectors. These are, with increasing radius: the Silicon Microvertex detector, the Central Vertex chamber, the Jet chamber and the Central Z chamber. Charged particle trajectories are reconstructed by the proper hit matching between the different tracking detectors.

### The Silicon Microvertex detector (SI)

The Silicon Microvertex detector consists of layers of semi-conducting silicon wafers each with many strips acting as reverse-biased junction diodes. When a charged particle passes through the junction, electron-hole pairs are produced. From the strip location where the charge is collected one single coordinate for the traversing particle is obtained. A second coordinate is obtained with hits in a second silicon layer having the strips perpendicular to those of the first one.

The particle impact parameter resolution is  $\sigma(d_0) = 15\mu\text{m}$  in the  $r$  plane. In the  $z$  plane the resolution is  $\sigma(z_0) = 20 - 50\mu\text{m}$ . [3] The Silicon Microvertex detector provides the most important information for all the studies involving secondary vertices reconstruction. That is the case of the present analysis where b quark jet tagging is necessary.

#### 2.1.1 The drift chambers

The Central Vertex chamber, the Jet chamber and the Central Z chamber are all drift chambers<sup>3</sup> located in the same pressure vessel inside the magnet coil, containing the same gas mixture at a pressure of 4 atm. A charged particle traversing the gas volume, releases electric charges by the ionization of the gas molecules. The released electric charge is accelerated towards the closest anode sense wire, due to the electric field created by the proper voltage setting of the anode wires and the cathodes. The accelerated charge causes further gas ionization and an avalanche charge multiplication occurs. A measure of the drift time from the initial ionization to the anode wire gives one spatial coordinate measurement of the traversing particle. The charge division, or the amount of charge collected at each end of the sense wire, gives an other spatial coordinate. The total charge collected is also a measurement of the energy lost  $dE/dx$  per unit length by the ionising particle. A precise measurement of  $dE/dx$  that can be obtained by multiple sampling (many sense wires) provides a good particle identification tool. The specific energy loss of particles is given by the Bethe-Bloch formula:

$$-\frac{dE}{dx} = Kz^2 \frac{Z}{A} \frac{1}{\beta} \left[ \frac{1}{2} \ln\left(\frac{2m_e c^2 \beta^2 \gamma^2 T_{max}}{I^2}\right) - \beta^2 - \frac{\delta}{2} \right] \quad (2.1)$$

where  $K = 4\pi N_A r_e^2 m_e c^2$ ,  $ze$  is the charge of the incident particle,  $Z$  is the atomic number of the medium,  $A$  being the atomic mass of the medium,  $\beta = \frac{v}{c}$  where  $v$  is the speed of the particle and

---

<sup>3</sup>A recommended book is [4]

$c$  the speed of light,  $m_e$  is the electron mass, and  $I$  is the mean excitation energy. [5]  $T_{max}$  is the maximum kinetic energy can be obtained by a single free electron in a single collision. It is given by:

$$T_{max} = \frac{2m_e e^2 \beta^2 \gamma^2}{1 + \frac{2\gamma m_e}{M} + (\frac{m_e}{M})^2} \quad (2.2)$$

Where  $M$  is the mass of the ionising particle through which the particle identification is possible.

### The Central Vertex chamber (CV)

The vertex detector is a 1 metre long, 470 mm in diameter, cylindrical drift chamber that surrounds the carbon fibre beam pipe and operates within the common 4 bar central tracking system pressure vessel. It is based on a scaled down jet chamber design. The chamber consists of an inner layer of 36 cells with axial wires and an outer layer of 36 small angle ( $4^\circ$ ) stereo cells.

The axial cells provide a precise measurement of position ( $\sigma = 50 \mu\text{m}$ ) in the  $r$ - $\phi$  plane to aid the measurement of secondary vertex topologies in  $e^+e^-$  annihilation events, while maintaining a good multi-hit detection capability to resolve individual particles within jets. Good drift time resolution is obtained by having 4 bar gas pressure and by limiting the maximum drift distance to reduce diffusion effects. A coarse measurement of the coordinate ( $z$ ) along the wire, by measuring the time difference between the signals from the two ends of the anode wire, is used in the fast track trigger and for offline track finding. The combination of stereo and axial cell information provides an accurate  $z$  measurement for charged particles close to the interaction region [2].

### The Jet chamber (CJ)

The jet chamber is designed to combine good space and double track resolution, essential for the efficient recording of jet-like events, with the possibility of particle identification, within a solid angle close to  $4\pi$ . The sensitive volume of the jet chamber is a cylinder with a length of about 4 m, surrounding the beam pipe and vertex detector. The outer diameter is 3.7 m, the inner 0.5 m. The chamber is subdivided into 24 identical sectors, each containing a plane with 159 sense wires. Cathode wire planes form the boundaries between adjacent sectors. All wires are parallel to the beam direction and the wire planes are radial. The maximum drift distance varies from 3 cm at the innermost sense wire to 25 cm at the outermost wire. In the range  $43^\circ < \theta < 137^\circ$  159 points are measured along each track, and at least 8 points on a track are obtained over a solid angle of 98% of  $4\pi$ . For each point true three-dimensional coordinates ( $r, \phi, z$ ) are determined from the wire position, the drift time and from a charge division measurement. The charge division method requires the measurement of the integrated charges for each hit at both ends of the signal wire. The ratio of these charges determines  $z$ , and their sum is used to calculate the energy loss  $dE/dx$  of the particle in the chamber gas.

The average resolution,  $\sigma_{r\phi}$ , is  $135 \mu\text{m}$  at the mean drift distance of 7 cm. The average resolution in  $z$ ,  $\sigma_z$ , is 6 cm. The momentum resolution obtained for  $e^+e^- \rightarrow \mu^+\mu^-$  is :  $\sigma_p/p^2 = 2.2 \times 10^{-3} \text{ GeV}^{-1}$ . In figure 2.3 the energy loss  $dE/dx$  is plotted as a function of momentum for tracks in a sample of multihadron events and events of the type  $e^+e^- \rightarrow \mu^+\mu^-$ . The figure indicates the clear capability of particle identification. Demanding at least 130 measurements per track a truncated mean is calculated providing a resolution,  $\sigma_{(dE/dx)}/(dE/dx)$ , of 3.8%.

### The Central Z chamber (CZ)

The Z-chambers are arranged to form a barrel layer around the jet chamber covering the polar angle from  $44^\circ$  to  $136^\circ$  and 94% of the azimuthal angle. They are designed to make precise measurements of the  $z$  coordinates of charged particles and to improve both the polar angle and invariant mass resolutions.

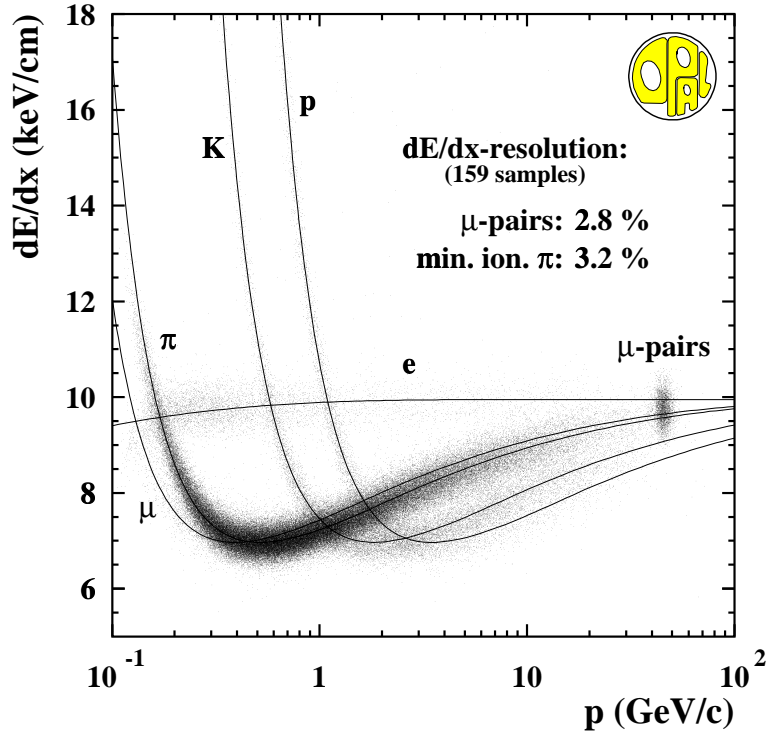


Figure 2.3: Particle identification by  $\frac{dE}{dx}$ .

The intrinsic  $z$  resolution, for minimum ionising particles normal to the drift direction, varies from less than  $100 \mu\text{m}$  at the shortest drift distances, to  $200 \mu\text{m}$  at the longest drift distances. The absolute resolution is determined by the precision of the survey, and is expected to be around  $300 \mu\text{m}$ . The  $r$ - $\phi$  resolution was measured to be of the order of  $1.5 \text{ cm}$ .

## 2.2 The Time-Of-Flight detector

The time-of-flight (TOF) system covers the barrel region  $|\cos\theta| < 0.82$ . It generates trigger signals and, by measuring the time of flight from the interaction region, allows charged particle identification in the range  $0.6$ - $2.5 \text{ GeV}$ . It also aids in the rejection of cosmic rays. The TOF detector consists of 160 scintillation counters forming a barrel of mean radius  $2.360 \text{ m}$  which is positioned outside and coaxial with the aluminium coil. Each counter is  $6.840 \text{ m}$  long and has a trapezoidal cross section ( $45 \text{ mm}$  thick,  $89$  to  $91 \text{ mm}$  wide). The time-of-flight resolution is  $350 \text{ ps}$ . [6]

## 2.3 The calorimeters

The calorimeters are designed to measure the particle energies by absorption. Most particles either slow down or stop in calorimeters and the energy they deposit is measured.

### The Electromagnetic Presampler detectors (PB & PE)

The Electro-magnetic Presamplers in the barrel and in the endcaps are designed to measure the energy loss of electro-magnetic particles (photons and electrons) that have showered before the electro-magnetic calorimeter. This measurement is used to improve the energy resolution of the electro-magnetic calorimeter. When a charged particle passes through the detector it ionises gas in

streamer tubes and anode wires inside the tubes collect the charge. On both sides of the tubes the signals induced in the cathode strips are read out. The angular resolution is  $\sigma \sim 2 \text{ m rad}$  and the resolution in the  $z$  plane is  $\sigma_z \sim 10\text{cm}$ , for a single charged particle. [2]

### The Electromagnetic Calorimeter detectors (EB & EE)

The Electromagnetic calorimeter detectors in the barrel and in the endcaps are designed to measure the energy of particles by absorbing their energy and converting it into visible light measured by photomultipliers. They are made out of lead-glass blocks that absorb almost all energy of  $e^\pm$ 's and  $\gamma$ 's while only a fraction of the energy of hadrons and muons is absorbed. The electromagnetic calorimeter measures both the position<sup>4</sup> and the energy of the particles reaching the detector. The typical electro-magnetic energy resolution is  $\frac{\sigma_E}{E} = 0.2\% + \frac{6.3\%}{\sqrt{E(\text{GeV})}}$ . [2]

### The Hadron Calorimeter detectors (HB, HE & HP)

The hadron calorimeters are mainly made of iron that absorbs the incoming hadrons through nuclear reactions. The active detectors are tubes filled with gas that are situated between layers of iron. In the tubes there is an anode wire that is read out. The measurements from the hadron calorimeters and the electromagnetic calorimeters combined are used to find the hadron energies. The hadron calorimeter is divided into 3 parts: the barrel and endcaps hadron calorimeters, the hadron poletip calorimeter and the forward calorimeters. The 3 parts differ only by size and position. The energy resolution of the 3 combined hadron calorimeters is varying from  $\sigma_E = \frac{100\%}{\sqrt{E(\text{GeV})}}$  to  $\frac{140\%}{\sqrt{E(\text{GeV})}}$  for hadron energies below 15 GeV to hadron energies at 50 GeV. [2]

## 2.4 Muon chamber and forward detector

### The Muon Chambers (MB & ME)

The muon chambers in the barrel and endcaps are drift chamber detectors. The purpose of the detectors is to identify muons, which are normally the only particles aside neutrinos which penetrate the hadron calorimeter and reach the muon chamber. The detectors consist of tubes filled with gas and an anode wire which is read out. The anode wires in the barrel detector are parallel to the  $z$  axis, while those in the endcaps are situated perpendicular to the  $z$  axis. The resolution for the barrel part in the  $\phi$  plane is  $\sigma = 1.5 \text{ mm}$  and in the  $z$  plane is  $\sigma_z = 2 \text{ mm}$ . The spatial resolution for the endcap part is  $\sigma = 3 \text{ mm}$  and in the perpendicular plane is  $\sigma \leq 1 \text{ mm}$ . [2]

### The Forward detector (FD)

The forward detector consists of 4 subdetectors; the Forward Calorimeter, the Tube Chambers, the Gamma Catcher and the Far-Forward monitors. The Forward calorimeter is a lead glass detector like the Electromagnetic calorimeter but with a presampler in front. See section 2.3 for a description of a presampler. The energy resolution is  $\frac{\sigma_E}{E} \sim \frac{17\%}{\sqrt{E(\text{GeV})}}$ . [2] The Tube Chambers consist of drift tubes used to measure the shower position. The shower position is found with an error  $\pm 3 \text{ mm}$ . [2] The gamma catcher is made of lead glass blocks and is read out by photo-diodes and is used to tag forward photons. The Far-Forward Monitors are lead-glass blocks which are situated on each side of the beam pipe, and read out by photomultipliers.

---

<sup>4</sup>The position is known since the position of the glass blocks is known.

### **The Silicon-tungsten luminosity meter detector (SW)**

The Silicon-tungsten detector is situated in the endcaps. It is a semiconductor detector made of silicon and tungsten strips and using the same particle detection principal as the Silicon Microvertex detector described in section 2.1. The purpose of the detector is to distinguish between Bhabha events used in the luminosity measurement and off-momentum electrons from the beam. Off-momentum particles come from either the beam itself or from interaction between the beam and the beam pipe or collisions between the beam particles and the residual air inside the beam pipe.

# Chapter 3

## The Electroweak Standard Model

The purpose of this chapter is to give a brief introduction to the Electroweak Standard Model. It will describe primarily some general theoretical ingredients relevant to the analysis, the Higgs boson and the Higgs mechanism of the Standard Model will be introduced.

The Standard Model is a gauge theory, meaning that the nature of the interactions in the theory is derived from the principle of gauge (or phase) invariance. This principle requires that the theory remains unchanged under certain local transformations. These transformations can be different for every space-time point. The transformations are described by certain symmetry groups; the three simplest symmetry groups (U(1), SU(2), SU(3)) seem to describe all experimental results so far.

### 3.1 Elementary particles

Elementary particles can generally be divided into two main groups according to their spin statistics: fermions with half integer spin and bosons with integer spin. The fermions are the particles that form matter and antimatter while the bosons mediate force.

#### Fermions

There are two kinds of elementary fermions, the quarks and the leptons. They occur in three generations as shown in table 3.1. The quarks are distinct from the leptons because they interact via the strong force while the leptons do not.

Fermions	1	2	3	Q	$T'^3$	Y	J
Quarks	up	charm	top	$2/3 e$	$1/2$	$1/3$	$1/2$
	down	strange	bottom	$-1/3 e$	$-1/2$	$1/3$	$1/2$
Leptons	$e^-$	$\mu^-$	$\tau^-$	$-1 e$	$-1/2$	$-1$	$1/2$
	$\nu_e$	$\nu_\mu$	$\nu_\tau$	0	$1/2$	$-1$	$1/2$

Table 3.1: The fermions.

Some of the characteristics of the fermions are the electric charge Q, the  $3^{rd}$  component of the weak isospin  $T'^3$ , the hypercharge Y and the total angular momentum or the spin J. To each fermion ( $e^-, u \dots$ ) exists an antifermion ( $e^+, \bar{u} \dots$ ) with the same mass and lifetime, but opposite charge. The quarks build hadrons that have flavours depending on which quarks they are made of; for example if a hadron has b-flavour -1(1) means that one of the valence quarks in the hadron is a  $b(\bar{b})$  quark. The flavour is conserved in strong and electromagnetic interactions, but not in weak interactions.



The only stable fermions are the ones from the first generation, and it is possible to measure the decay of the s-, c- and b-quarks.[5]

If the projection of the spin vector on the momentum vector of the particle is positive its helicity is equal to 1, and if they are in opposite direction its helicity is -1. The handedness of the particles equals helicity in the massless limit, where Right handed particles correspond to helicity 1 and Left handed to helicity -1.[7] Experimentally only Left handed neutrinos are observed (parity violation in the weak processes).

The Heisenberg uncertainty principle gives a relationship between the lifetime of a particle and its energy  $\Delta E \geq \frac{\hbar}{\Delta t}$  [8]. If the particle has a very short lifetime, too short to be measured, the width is used to describe the particle instead. The width is the total width of the mass distribution that is given by  $\Gamma = \frac{\hbar}{\tau}$  where  $\tau$  is the lifetime of the particle.

The lifetime of a particle depends on the type of force causing the decay (strong or electroweak). A weak decay, a decay via a  $W^+, W^-$  or a  $Z^0$  boson, results in a long lifetime with respect to other decays. The electromagnetic decay, a decay via a photon gives a shorter lifetime and the shortest lifetimes normally come from strong decays. This can be also explained by the available decay phase space, the bigger the volume of the phase space of the decay products (due to energy and momentum conservation) the shorter the lifetime  $\tau$  of the decaying particle. If there are many decay modes, the lifetime is smaller compared to if there exist only a few decay modes. For example in the  $\tau$  and  $\mu$  decays, the  $\tau$  decays faster than the  $\mu$  partly because there are more decay modes available for the  $\tau$  in comparison to just one possible decay mode for the  $\mu$ .

## Bosons

The bosons are the particles that mediate force, both the electroweak and the strong force. Table 3.2 shows the observed electroweak bosons and the force they represent.

Boson	Force	Mass	Charge	J
$Z^0$	electroweak	arbitrary	0	1
$W^-W^+$	electroweak	arbitrary	$\pm 1e$	1
$\gamma$	electroweak	0	0	1

Table 3.2: The electroweak bosons in the Electroweak Standard Model.

Some of the properties for the bosons are the electric charge Q, the total angular momentum or the spin J, their masses and the force (the interaction they mediate). In addition to the electroweak bosons there are the gluons that mediate the strong force. The bosons mentioned have all spin 1 and are therefore called vector bosons. The massive  $W^+, W^-$  and  $Z^0$  and the massless  $\gamma$  bosons mediate the electroweak force and the massless gluons belong to the strong force. The masses of the  $Z^0$  and the  $W^-W^+$  bosons are  $91.2 \pm 0.007$  GeV and  $80.4 \pm 0.10$  GeV respectively.[5]

## Properties of the particles

The boson exchanged in electroweak interactions can be one of the two charged massive bosons  $W^+, W^-$ , the neutral massive  $Z^0$  or the massless photon. The difference between the massive bosons and the photon is that the massless  $\gamma$  boson can mediate the electroweak force over infinite distances while the  $W^+, W^-$  and the  $Z^0$  only can transmit the electroweak force over a distance in the order of  $10^{-18}$  meters.

The analogy of charge for the strong force is called ‘‘colour’’. Quarks can have 3 different colours (red, blue and green) and anti-colours (anti-red, anti-blue and anti-green). The gluons carry colour

charges themselves in the way that for example a green up-quark becomes red by absorbing a red-anti-green gluon. No isolated single quark is observed, they quarks build colour singlet states, the so called hadrons.

The strong force is weaker the closer the particles are to each other. This property of the strong force is referred to as asymptotic freedom. In a hadron there are either two or three valence quarks, which are held together by the strong force which is mediated by the gluons. The further away the quarks are from each other the stronger the force is, and the closer the quarks are the more they behave like free particles. [9, 7]

The strength of interactions is expressed by coupling constants, which vary depending on the type of interaction and the momentum transfer. This dependence on momentum transfer is usually referred to as the running of the coupling constants. Particles that mediate an interaction are called virtual if they are off mass shell which means the mass of the particle, calculated within the interaction process, is not equal to the rest mass of the particle:  $E^2 - p^2 \neq M_{rest}^2$ . [7]

In addition to the observed bosons mentioned above there is one still unobserved boson in the Standard Model: the Higgs boson.

## 3.2 The Higgs bosons in the Standard Model

For every interaction process a Lagrangian,  $\mathcal{L}$ , from which the involved particles dynamics can be derived, shall be written. The Lagrangian of a system is the difference between the kinetic and the potential energy. The system's dynamics is obtained by applying the action principal that states that the integral of the Lagrangian over all the system variables should be extremal.

The requirement of the Lagrangian to be invariant under local phase (gauge) transformations makes it necessary to include fields and their derivatives. These fields are identified with the gauge bosons, the 4 bosons of the electroweak theory. To get non vanishing masses for the heavy bosons without losing gauge invariance of the Lagrangian one introduce the so-called Higgs mechanism. The symmetric Higgs field that is included has continuous ground states that are not zero. By choosing one out of these ground states one loses the symmetry the Higgs potential itself has. This is the spontaneous symmetry breaking that leads to mass terms for some of the bosons observed in nature. The number of mass terms in the Lagrangian matches the number of massive bosons that are found experimentally (without the Higgs boson).[10, 11, 12]

### 3.2.1 The Higgs mechanism

In the following some of the calculations leading to this spontaneous symmetry breaking, also referred to as the Higgs mechanism, will be shown.

#### The U(1) symmetry group

The U(1) symmetry group is the invariance under the global phase transformation

$$\begin{aligned} \partial_\mu \psi &\rightarrow e^{i\alpha} \partial_\mu \psi \\ \bar{\psi} &\rightarrow e^{-i\alpha} \bar{\psi} \end{aligned} \quad (3.1)$$

where  $\alpha$  is a real constant[10].  $e^{i\alpha}$  is the phase transformation (rotation) leaving the Lagrangian invariant. Noether's theorem states that invariance under symmetry group leads to a conservation law. For example, invariance under U(1) leads to the conservation of the electric charge. The next step is to extend the idea of global gauge invariance to local gauge invariance with a non constant phase  $\alpha = \alpha(\vec{x}, t)$ . The derivative of the phase transformation must transform so it does not depend

on coordinate. The derivative  $D_\mu$  that transforms covariantly under phase transformation is given by

$$D_\mu\psi \rightarrow e^{i\alpha(x)}D_\mu\psi \quad (3.2)$$

In order for the Lagrangian to be invariant under this local gauge transformation, a vector field is included in the Lagrangian. The vector field, referred to as the gauge vector field, cancels out the non invariant terms in the Lagrangian. [10] The derivative which satisfies this is given by:

$$D_\mu \equiv \partial_\mu - ieA_\mu \quad (3.3)$$

where  $e$  is the coupling constant. The corresponding transformation of the vector field is given by

$$A_\mu \rightarrow A_\mu + \frac{1}{e}\partial_\mu\alpha \quad (3.4)$$

Thus the requirement of local gauge invariance leads to a Lagrangian containing the photon field with the form of its interaction specified. This makes it necessary to include a term in the Lagrangian to take into account the photon's kinetic energy. The term should be gauge invariant and it is the field strength tensor. [10] This tensor is given by

$$F_{\mu\nu} = \partial_\mu A_\nu - \partial_\nu A_\mu \quad (3.5)$$

from which Maxwell's equations can be obtained. The Lagrangian thereby becomes

$$\mathcal{L} = \bar{\psi}(i\gamma^\mu\partial_\mu - m)\psi + e\bar{\psi}\gamma^\mu A_\mu\psi - \frac{1}{4}F_{\mu\nu}F^{\mu\nu} \quad (3.6)$$

which is the Lagrangian of the theory of Quantum Electro Dynamics (QED). It can be seen that, by requiring the Lagrangian to be invariant under phase transformation, gauge invariance leads to a massless gauge field, the photon.[10]

### The $SU(2)_L \otimes U(1)_Y$ symmetry group

The  $SU(2)_L$  symmetry group is a different and larger symmetry group of left-handed particles and it predicts a  $W^1$ , a  $W^2$  and a  $W^0$  boson. The  $U(1)_Y$  group predicts a gauge field corresponding to a  $B^0$  boson.  $SU(2)_L$  symmetry of weak isospin combined with  $U(1)_Y$  symmetry of hypercharge provide the foundation of the electroweak theory. The prediction of the fields and the way they couple to matter arises from the same principle of local gauge invariance described in the previous section, although the details of the gauge transformations for  $SU(2)_L$  are slightly more complicated than for  $U(1)_Y$ .

The combination of  $SU(2)_L$  and  $U(1)_Y$  is needed because in experiments the  $Z^0$  boson cannot be identified with any of the the  $SU(2)_L$ 's  $W$  bosons. When combining the two symmetry groups with spontaneous symmetry breaking the four new fields correspond to the experimentally found bosons,  $W^-, W^+, Z^0$  and  $\gamma$ . Two of the bosons, the  $W^+, W^-$ , are from the  $SU(2)_L$  symmetry group, and the two other bosons  $Z^0$  and  $\gamma$  originate from mixing between the two groups  $SU(2)_L$  and  $U(1)_Y$ . The  $\sin^2(\theta_W)$  is the weak mixing angle that determines the mixing of the transformations groups  $SU(2)$  and  $U(1)$  that form the electroweak theory. This unification of the electromagnetic and the weak part of the Standard Model is due to the fact that a combination of the field of the  $U(1)_Y$  with the neutral field of the  $SU(2)_L$  group leads to the observed photon and  $Z^0$  boson. [7, 10]

### The Higgs mechanism

The problem with the simplest version of a  $SU(2)_L \otimes U(1)_Y$  Lagrangian is that it does not have any mass terms for the  $W^+, W^-, Z^0$  bosons. The Higgs mechanism was introduced to include mass terms

to the Lagrangian and still preserve the properties of local gauge invariance and renormalisability. Renormalisability means that amplitudes can be calculated at all orders of the coupling constants.<sup>1</sup> The local gauge invariant Lagrangian is given by:

$$\mathcal{L} = (\partial^\mu + ieA^\mu)\phi^*(\partial^\mu - ieA_\mu)\phi - \mu^2\phi^*\phi - \lambda(\phi^*\phi)^2 - \frac{1}{4}F_{\mu\nu}F^{\mu\nu} \quad (3.7)$$

where  $\mu$  and  $\lambda$  are free real constants describing the Higgs potential. In the case of  $\mu^2 < 0$  the desired mass term is included in the Lagrangian. The added gauge field has a local maximum at the field equal to zero, but a continuum of stable minima for the field not equal to zero. Only one minimum from this continuum occurs to be the observed ground state, this is the spontaneous symmetry breaking.[10] The Lagrangian including mass terms for the bosons is given by

$$\mathcal{L} = \frac{1}{2}(\partial_\mu h)^2 - \lambda v^2 h^2 + \frac{1}{2}e^2 v^2 A_\mu^2 - \lambda v h^3 - \frac{1}{4}\lambda h^4 + \frac{1}{2}e^2 A_\mu^2 h^2 + v e^2 A_\mu^2 h - \frac{1}{4}F_{\mu\nu}F^{\mu\nu} \quad (3.8)$$

where  $v$  is the field at the chosen minimum,  $\lambda$  is the coupling between the field and the scalar particle,  $A_\mu$  is a vector gauge boson and  $h$  is the massive scalar that is the Higgs boson.[10] The coupling  $\lambda$  is not predicted and must be found experimentally. The Higgs coupling is proportional to the mass of the particles involved.

The Higgs boson, in the standard model, should occur as a scalar neutral physical particle. The mass of the Higgs boson is not predicted by the theory, therefore one can only determine its mass experimentally. The coupling to the Higgs boson is stronger for particles with higher masses[13, 10].

### 3.2.2 The Standard Model Higgs decay

The main production modes of the Standard Model Higgs boson in  $e^+e^-$  collision are Higgsstrahlung,  $Z^0Z^0$  and  $W^-W^+$ -fusion. The Higgsstrahlung process is  $e^+e^- \rightarrow Z^* \rightarrow Z^0H$ . The  $Z^0Z^0$  fusion or  $W^-W^+$  fusion will produce the Higgs boson in the following way:  $e^+e^- \rightarrow e^+e^-Z^0Z^0 \rightarrow e^+e^-H$  or  $e^+e^- \rightarrow \nu_e\bar{\nu}_eW^-W^+ \rightarrow \nu_e\bar{\nu}_eH$ . The production mode depends on the centre-of-mass energy and the cross sections. At energies achievable at LEP, the Standard Model Higgs is expected to be produced predominantly via Higgsstrahlung. [14, 15].

The cross section of the Standard Model Higgs boson is given by

$$\sigma = \frac{\pi\alpha^2}{8\sqrt{s}} \frac{K(K^2 + 3M_Z^2) \cdot (1 + (1 - 4x_W)^2)}{(s - M_Z^2)^2 \cdot x_W^2(1 - x_W)^2} \quad (3.9)$$

where  $K$  is the Higgs bosons momentum in the rest frame of the colliding electron and positron and  $x_W \equiv \sin^2(\theta_W)$  the weak mixing angle [13]. The cross section therefore depends on the momentum and thus the mass of the particle. The current analysis has been done for the Standard Model Higgs boson produced via Higgsstrahlung, other production modes will not be discussed.

In the Higgsstrahlung process the Higgs boson has many different possible decay channels including leptonic, hadronic and two photons decay. Some of the Higgs bosons different decay modes and their signature in the data are the following [16]:

$$e^-e^+ \rightarrow Z^* \rightarrow HZ^0 \rightarrow H \rightarrow b\bar{b}, Z^0 \rightarrow q\bar{q} \quad 4 \text{ jet event} \quad (3.10)$$

$$\rightarrow H \rightarrow b\bar{b}, Z^0 \rightarrow l\bar{l} \quad 2 \text{ jets and 2 leptons} \quad (3.11)$$

$$\rightarrow H \rightarrow l\bar{l}, Z^0 \rightarrow q\bar{q} \quad 2 \text{ leptons and 2 jets} \quad (3.12)$$

$$\rightarrow H \rightarrow l\bar{l}, Z^0 \rightarrow \nu\bar{\nu} \quad \text{missing energy and 2 leptons} \quad (3.13)$$

$$\rightarrow H \rightarrow q\bar{q}, Z^0 \rightarrow \nu\bar{\nu} \quad \text{missing energy and 2 jets} \quad (3.14)$$

---

<sup>1</sup>This was proven by Gerardus 't Hooft and Emeritus Martinus J.G. Veltman.

At the current centre-of-mass energies at LEP, the dominant decay mode is the 4-jet channel.

The figure 3.1 shows standard model Higgs branching ratios as a function of the Higgs mass. At a centre-of-mass energy of 189 GeV and for Higgs masses around the  $Z^0$  boson mass the Higgs decay is dominated ( $> 80\%$ ) by the  $b\bar{b}$  channel.

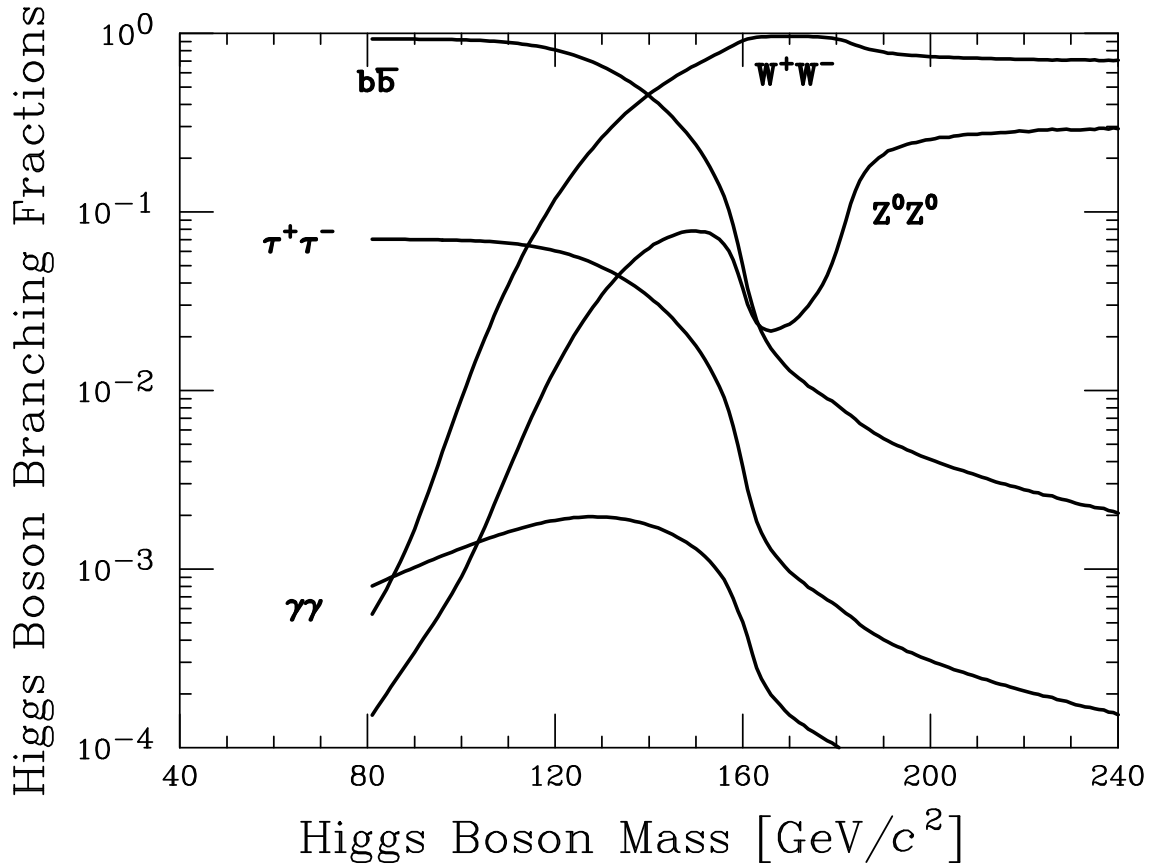


Figure 3.1: The Higgs mass versus the branching ratios [17].

The high branching ratio for the Higgs to  $b\bar{b}$ -pair makes the 4-jet channel, for which the first order Feynman graph is shown in figure 3.2, a good channel to search for the Higgs.

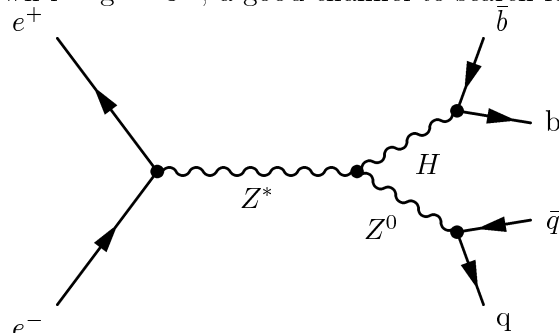


Figure 3.2: The first order Feynman diagram

However, the 4-jet channel is dominated by the the standard model backgrounds  $W^-W^+$ ,  $Z^0Z^0$  and the QCD  $e^+e^- \rightarrow q\bar{q} \rightarrow 4jets$ . In this analysis the  $ZZ$  background is not reducible since it has the same signature as the searched channel.

# Chapter 4

## The Analysis

The analysis is performed on the full OPAL data sample recorded at the centre-of-mass-energy of 189 GeV. This corresponds to a total integrated luminosity of  $\mathcal{L} = 172.1 \text{ pb}^{-1}$  obtained after having required a good detector status for the Silicon Microvertex detector, all the central tracking drift chambers, the electromagnetic calorimeters and the hadron calorimeters.

### 4.1 Selection of events

Preselection cuts are applied on events to reject obvious non 4-jet events consisting mainly of  $\gamma\gamma$  events. The following, rather loose, criteria are required for each event in order to be selected for further processing: the total measured visible energy of the event should exceed 100 GeV. The jet finder algorithm is forced to resolve 4 jets in the event for which the number of charged particles in each jet should be larger than three, the energy of each jet must be larger than 5 GeV, and each jet should have a  $\sin(\theta_{beam})$  larger than 0.95 which corresponds to an angle of  $18^\circ$  between the beam and the jet direction.

When applied on Monte Carlo generated events, these preselection cuts remove 97% of the  $\gamma\gamma$  events, 79% of the qq ( QCD like) events and 9.8% of the the standard 4 fermions qq $\bar{q}\bar{q}$  (non Higgs) events. For the Monte Carlo  $H \rightarrow all Z \rightarrow q\bar{q}$  process, the preselection cuts remove 8.8% and 10.5% events for the events generated with  $M_H = 90 \text{ GeV}$  and  $M_H = 95 \text{ GeV}$  respectively. These rejected  $HZ^0$  events correspond mainly to the case where the  $H$  decays into 2 leptons.

#### 4.1.1 The jet finder

There are several algorithms that reconstruct jets in an event. The algorithms use different schemes to combine particles (i.e. tracks or non associated electromagnetic clusters) into jets. Depending on the algorithm and the centre-of-mass energy one obtains slightly different energy and angular resolutions for the reconstructed jets. In this analysis among the algorithms that have been compared, the LUCCLUS [18] jet finder was found to produce a better angular resolution, that is for example more than 5% better than in the case of the commonly used Durham [19] jet finder [20]. A good angular resolution is of utmost importance for the kinematic fit, as the jet direction reconstructed by the jet finder algorithm will be assumed to be correct.

Therefore in the current analysis the LUCCLUS jet finder is used. LUCCLUS uses a resolution parameter  $y_{ij}$  to combine the particle i and j to one particles [18]. This parameter is somehow related to the invariant mass of the two particles and is defined as:

$$y_{ij} \approx \frac{|\vec{p}_i \times \vec{p}_j|}{|\vec{p}_i + \vec{p}_j|} \quad (4.1)$$

Before combining two particles into another particle (jet), the  $y_{ij}$  is evaluated. The particles are combined into one, by summing up the corresponding 4 vectors, if  $y_{ij}$  is found to be smaller than a fixed resolution parameter  $y_{cut}$ . The combination process is repeated until no pair of particles or jets satisfies the above condition. To force the algorithm to produce 4 jets, the value of  $y_{cut}$  is varied (increased) to allow the combination process to proceed again. The iterations are stopped when 4 jets are obtained. The algorithm always finds 4 jets provided that the number of particles in the event is at least 4. Values of  $y_{cut}$  where the event switches from  $N$  to  $N - 1$  jets are an indication of how stable the event is as an  $N$ -jet event. The number of jets will decrease with increasing value of  $y_{cut}$ . The value of  $y_{cut}$  where the obtained number of jets will switch from 4 to 3 jets is called  $y_{34}$ , and  $y_{45}$  is the value where the number of jets switches from 5 to 4 jets. The distance  $y_{34} - y_{45}$  is therefore an evaluation of how much the event is topologically stable as a 4-jet event. A large value of this distance indicates a better separation of the jets (cleaner topology).

In order to understand how the jet energy and angular resolution is affected by the hadronisation process and the detector resolution Monte Carlo events are used. The initially generated partons are matched angularly to the hadron level. The hadron level is the level where the parton shower stops and particles emerge and the jet finder is applied to the emerging hadrons. The same angular matching is performed between the hadron level jets to the detector level jets. The detector level corresponds to the level where the OPAL detector response is fully simulated for all the particles produced at hadron level. Thus the parton to detector level matching provides a way to estimate the resolution on the final reconstructed jet parameters at the detector level. To be explicit, the angles between the jets from one level to the next are calculated, these are all the possible angles between the partons and the hadron jets and the angles between the hadron jets and the detector jets. The jets on hadron level are taken to be the reference jets to the jets on parton and detector level, and a hadron level jet matches unambiguously one parton level jet and one detector level jet, those making the smallest angle to the considered hadron jet direction.

## The energy and angular resolution

The resolution of the measured jet quantities is estimated by comparing parton level with detector level informations. It is an important ingredient in the constrained kinematic fit procedure that will be applied later to further discriminate between background and signal events. The resolution information, if estimated on event by event basis, can also be used to reject events with badly reconstructed jets.

The jet energy resolution is defined by subtracting parton level jet energy from detector level jet energy. It can only be calculated for Monte Carlo events since only here the parton level information is available. The energy resolution is given by

$$\sigma_E = \left\langle \frac{E_{jet}^{measured} - E_{jet}^{true}}{E_{jet}^{true}} \right\rangle \quad (4.2)$$

where  $E_{jet}^{true}$  is the initial parton generated energy and  $E_{jet}^{measured}$  is the corrected energy for the corresponding jet at detector level. The corrected detector level jet energies are obtained by imposing energy and momentum conservation on the full event (referred to as 4C-fit), assuming massless jets and considering that the reconstructed jet directions are correct. The resolution of the three momentum component of the jet are defined similarly to the energy resolution. Here we should mention that at parton level, the information concerning the original four quarks for  $H \rightarrow q\bar{q}$  and  $Z^0 \rightarrow q\bar{q}$  decays is missing because of an error in the storage of the generated Monte Carlo information. To cope with this error, the jet finding is performed at parton level on the partons remaining at the end of the parton shower. The energy of the parton jet is assumed to be correct and is used in the definition of the energy resolution. In principle the resolution on the jet parameters

(i.e. energy and momentum) for the 4-jet events, at a fixed centre-of-mass-energy, should not depend too much on whether the event originates from a  $HZ^0$ ,  $W^-W^+$  or  $Z^0Z^0$  event given that we are aiming for a Higgs mass in the close neighbourhood of the  $Z^0$  boson. Therefore, we also used the large available  $W^-W^+$  Monte Carlo sample, that has all the initial parton level information available, to evaluate the resolution of the jet parameters.

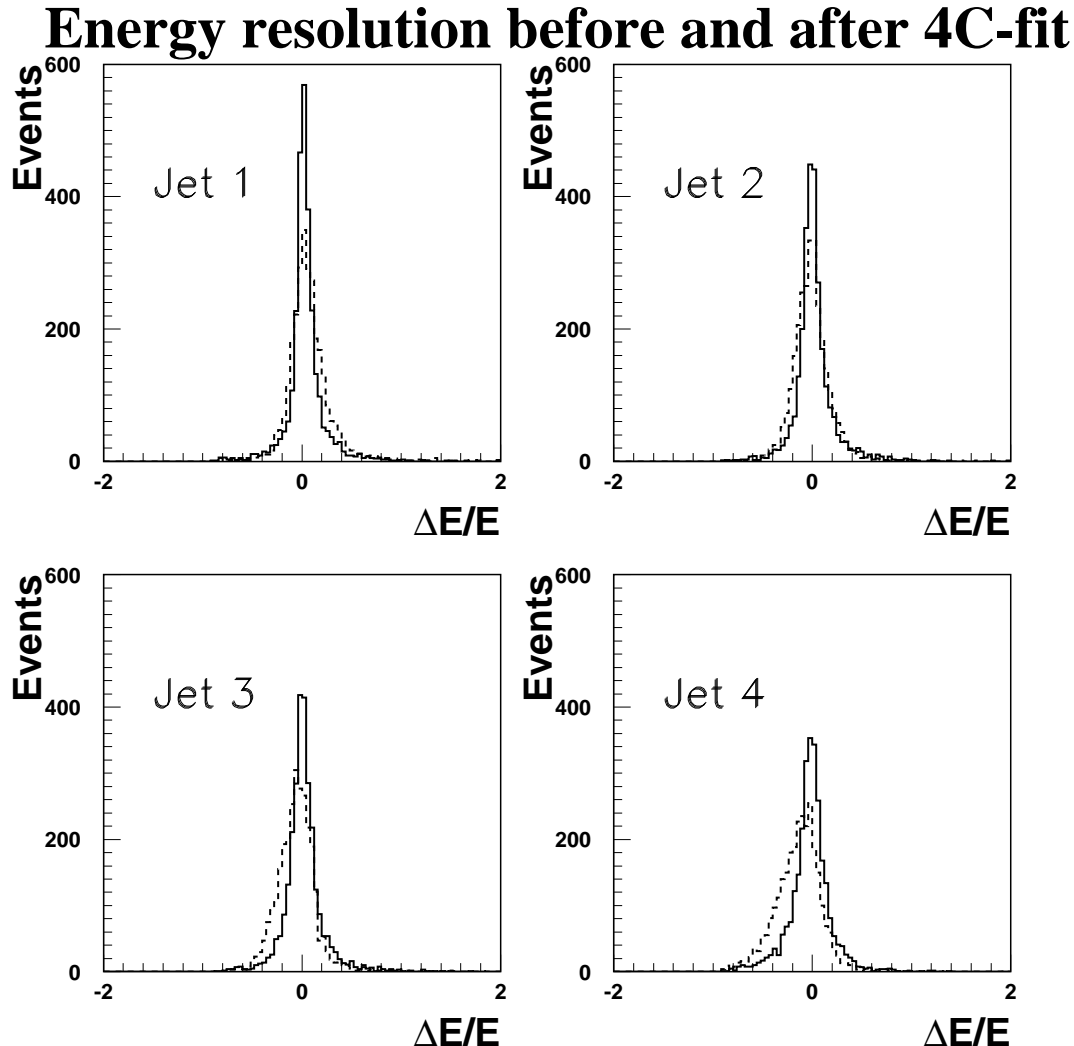


Figure 4.1: Distributions of the relative energy error.

In figure 4.1 we see how the 4C-fit mentioned above increases the jet energy resolution: the dashed lines show the energy resolution before the correction and the solid lines after the 4C-fit correction has been applied. The energy resolution is better after the constraints on energy and momentum conservation are satisfied as expected. The jets are energy ordered with jet 1 being the jet with the highest energy. The energy resolutions of jet 1 and jet 2 are symmetric distributions around 0 before and after the 4C-fit. The distributions for jet 3 and 4 show non symmetric tails due to badly reconstructed jets before the 4C-fit, these are partially removed after the 4C-fit.

In the table 4.1.1 the width of the energy resolution  $\sigma_E$  distributions are shown for the Monte Carlo samples with generated Higgs mass at 90 GeV and at 95 GeV, this summarises the improve-



Higgs Mass	Sigma	Jet 1	Jet 2	Jet 3	Jet 4
90 GeV	Before the 4C-fit	0.1527	0.1590	0.1651	0.2039
	After the 4C-fit	0.08626	0.1108	0.1229	0.1471
95 GeV	Before the 4C-fit	0.1583	0.1449	0.1569	0.2069
	After the 4C-fit	0.1244	0.1505	0.1521	0.1690

Table 4.1: Energy resolution.

ments of the 4C-fit on the jet energy resolutions.

### The angular resolution

The angular resolution is defined as the angle between the direction of the initial parton and the corresponding jet at detector level. Detector effects and assignment of particles to the wrong jets by the jet algorithm are the main contributions to the angular resolution. However, for the Monte Carlo events a wrong matching between the initial parton and the detector jets contributes also. Thus the jet angular resolution will be somehow underestimated. The angular resolution is given (after the parton to detector level jet correspondence is established by angular matching) by:

$$\Delta\theta = \langle \text{acos}\left(\frac{\vec{p}_{\text{detector}} \cdot \vec{p}_{\text{parton}}}{|\vec{p}_{\text{detector}}| \cdot |\vec{p}_{\text{parton}}|}\right) \rangle \quad (4.3)$$

The angular resolution is expected to be different for the four jets since they are energy ordered. The most energetic jet is expected to have the best angular resolution. This is due to low momentum particles that are lost or assigned to the wrong jet and this effect is expected to be larger in the least energetic jet.

The angular resolution distributions  $\Delta\theta$  are shown in figure 4.2 separately for each of the four energy ordered jets. The angles between the directions of the jets are smallest in jet 1 as expected, and the largest angle is in jet 4. All the angular distributions have a maximum close to  $3^\circ$  and a small tail. It indicates that the angular matching procedure is indeed a successful way of matching jets between parton and detector levels.

Higgs Mass		Jet 1	Jet 2	Jet 3	Jet 4
90 GeV	mean	2.446°	2.651°	2.874°	3.527°
95 GeV	mean	2.405°	2.634°	2.819°	3.233°

Table 4.2: The angular resolution

Table 4.1.1 shows the mean values of the angular resolution distribution. The results quoted are for the Monte Carlo events generated with the Higgs mass at 90 GeV and 95 GeV. These values are not affected by the 4C-fit because these are assumed to be correct in the procedure.

## 4.2 Likelihood classification of events

Here the aim is to produce a single probability-like variable able to discriminate between signal and background events. This variable is referred to as a likelihood since it is generally defined as a product of a set of probabilities, each defined for one single variable as the ratio between signal and signal plus background frequency. In the ideal case, where the event can be defined with a set of  $N$  independent variables  $v_i$ , and where for each variable the probabilities  $P_{s_{v_i}}$  for being signal and

# Angular resolution

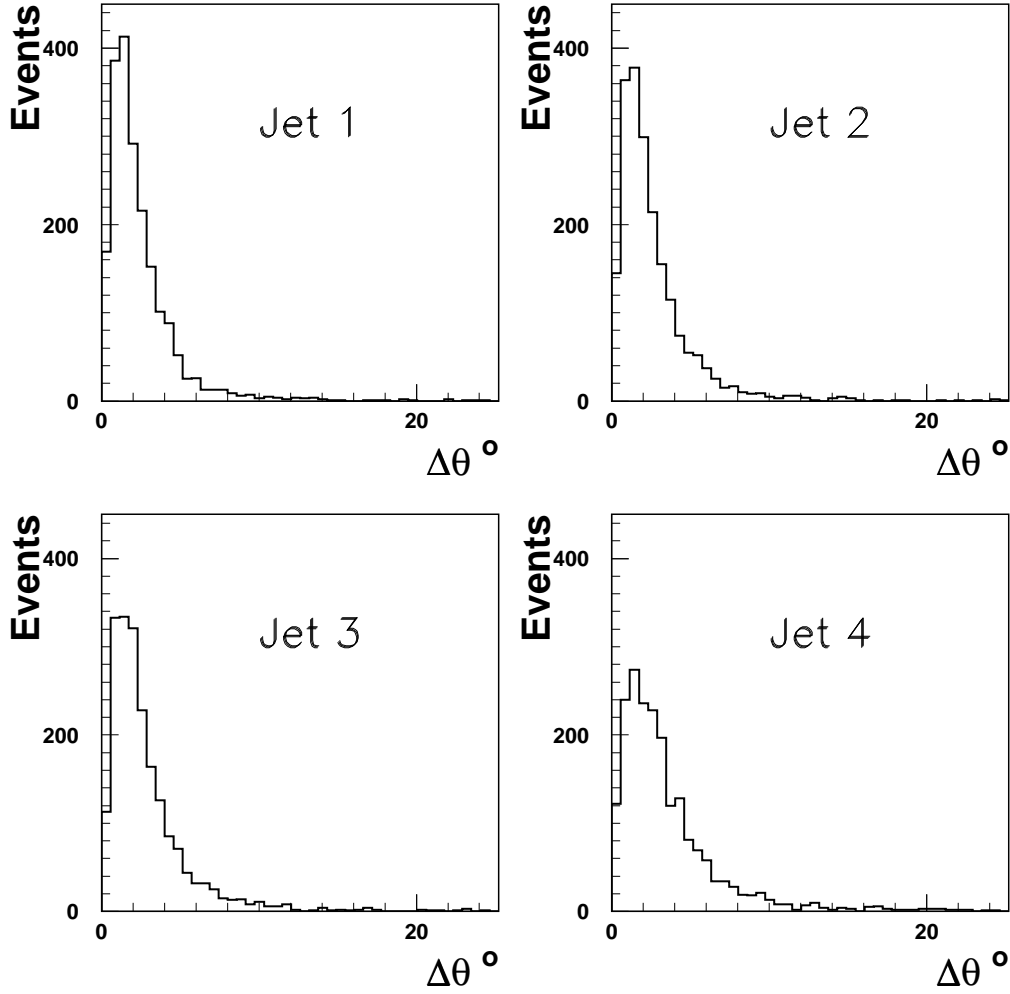


Figure 4.2: The distributions of the error  $\Delta\theta$  on the measurement of the jet directions.

$Pb_{v_i}$  for being background are known, the total probabilities for signal and background are then defined as following:

$$P_{signal} = P_{s_{v_1}} \cdot P_{s_{v_2}} \cdot P_{s_{v_3}} \dots P_{s_{v_n}} \quad (4.4)$$

$$P_{background} = Pb_{v_1} \cdot Pb_{v_2} \cdot Pb_{v_3} \dots Pb_{v_n} \quad (4.5)$$

The normalised likelihood for a signal event is then given by :

$$\mathcal{L} = \frac{P_{signal}}{P_{signal} + P_{background}} \quad (4.6)$$

The advantages of a likelihood based selection method in comparison to a cut-based analysis is that an event that looks like a good event except in one requirement/cut will be rejected in a cut-based analysis where it might be accepted in a likelihood procedure. A cut on the likelihood to define the final event sample uses the full information in the  $N$ -dimensional space of the input variables, that is unlike successive cuts on single variables or projections for which each time the information concerning the  $N - 1$  other variables is somehow hidden.

### 4.2.1 Likelihood input variables

We are aiming to discriminate between the 4 jet events that are produced from two different sources: the signal sources and the background sources. The signal sources are the processes where a  $Z^0$  boson decaying into 2 hadronic jets is produced together with two other jets preferably tagged as b quark jets, these are the standard  $Z^0 Z^0$  and the  $H Z^0$  processes. The background sources consist of any other process that leads to 4 hadronic jets in the final state, these are dominantly the WW pair production and the  $q\bar{q}$  QCD processes. We found that four adequately chosen variables are enough to perform a good discrimination between signal and background processes. The first variable  $P_k$  is the output of a constrained kinematic fit, that is the probability for an event to have 2 jets coming from a  $Z^0$  boson decay times the probability to have no  $W^-W^+$  pair in the event. As will be described later, this kinematic probability contains inputs from several kinematic related variables. The variable  $P_k$  should be optimised against  $W^-W^+$  like events.

The second variable  $P_b$ , concerns the probability to have two jets among the four, each coming from a b quark fragmentation. This should give a bigger weight for signal like events. The third variable is derived from the event's thrust (defined later)  $P_t$  that acts as a powerful discriminator against QCD like  $q\bar{q}$  events. The last variable denoted  $P_y$ , is obtained from the distance  $y_{34} - y_{45}$  that concerns the event stability as a 4 jet event. This variable acts against QCD  $q\bar{q}$  events and also against the events with a confusing topology, i.e. events where many jets are close to each other and where assigning particles to jets becomes a hard task.

## 4.3 The kinematic variable $P_k$

This variable is the output of the constrained kinematic fit described below.

### 4.3.1 Constrained fit procedure

The procedure is derived for the general case where we have  $N_{jet}$  jets and we wish to impose, in addition to the energy-momentum conservation constraints (4-C), additional constraints on di-jet invariant masses or any other constraint on a single or a combination of jets.

Each jet  $j$  is defined with a set of 4 initial measured variables  $X_i^{j0}$   $i = 1$  to 4 and their error measurements  $\sigma_i^j$ . We want to find a new set of variables  $X_i^j$  that minimises the quantity:

$$\chi^2 = \chi_0^2 - 2 \sum_{(\alpha,\beta)} \lambda_{(\alpha,\beta)} (M_{(\alpha,\beta)}^2 - M_{(\alpha,\beta)}^{2,th}) - 2 \sum_{c=1}^4 \lambda_c (F_c^2 - F_c^{2,th}) \quad (4.7)$$

Here

$$\chi_0^2 = \sum_{j=1}^{N_{jet}} \sum_{i=1}^4 \left( \frac{X_i^j - X_i^{j0}}{\sigma_i^j} \right)^2 \quad (4.8)$$

is the usual  $\chi^2$  that is minimal for  $X_i^j = X_i^{j0}$ . The sum  $\sum_{(\alpha,\beta)}$  runs over all the di-jet pairs  $(\alpha, \beta)$  (can be anything else) for which we want to constrain the measured quantity  $M_{(\alpha,\beta)}^2$  to be equal to the fixed quantity  $M_{(\alpha,\beta)}^{2,th}$ . The sum  $\sum_c$  stands for the 4 energy and momentum conservation constraints:

$$F_c^2 = \left( \sum_{\ell=1}^4 X_c^\ell \right)^2 \quad \text{and} \quad F_c^{2,th} = (\sqrt{S})^2 \delta_{c,4} \quad (4.9)$$

The  $\lambda$  coefficients are the usual Lagrange multipliers. The  $\chi^2$  is minimal if all the partial derivatives

$\frac{\partial X^2}{\partial X_i^j}$  are equal to zero. That leads to :

$$\Delta X_i^j = \sigma_i^j \left( \sum_{(\alpha,\beta)} \lambda_{(\alpha,\beta)} \frac{\partial \Delta M_{(\alpha,\beta)}^2}{\partial X_i^j} + \sum_c \lambda_c \frac{\partial \Delta F_c^2}{\partial X_i^j} \right) \quad (4.10)$$

where

$$\Delta X_i^j = X_i^j - X_i^{j0} \quad (4.11)$$

$$\Delta M_{(\alpha,\beta)}^2 = M_{(\alpha,\beta)}^2 - M_{(\alpha,\beta)}^{2,th} \quad (4.12)$$

$$\Delta F_c^2 = F_c^2 - F_c^{2,th} \quad (4.13)$$

At the first order and around the initial point  $X_p^{q0}$  one could write

$$\Delta M_{(\alpha,\beta)}^2 = \sum_p \sum_q \frac{\partial \Delta M_{(\alpha,\beta)}^2}{\partial X_p^q} \Delta X_p^q \quad (4.14)$$

$$\Delta F_c^2 = \sum_p \sum_q \frac{\partial \Delta F_c^2}{\partial X_p^q} \Delta X_p^q \quad (4.15)$$

By replacing in these last two equations  $\Delta X_p^q$  by its expression from 4.10 we obtain the following set of linear equations :

$$\Delta M_{(\alpha,\beta)}^2 = \sum_{(m,n)}^{all \ cconstraints} \lambda_{(m,n)} \vec{W}_{(\alpha,\beta)} \vec{W}_{(m,n)} + \sum_a \lambda_a \vec{W}_{(\alpha,\beta)} \vec{V}_a \quad (4.16)$$

$$\Delta F_c^2 = \sum_{(m,n)}^{all \ cconstraints} \lambda_{(m,n)} \vec{W}_{(m,n)} + \sum_a \lambda_a \vec{V}_a \vec{V}_c \quad (4.17)$$

where

$$\vec{W}_{(\alpha,\beta)} = \left( \frac{\partial \Delta M_{(\alpha,\beta)}^2}{\partial X_i^j} \sqrt{\sigma_i^j}, \dots, \quad i = 1, 4 \text{ and } j = 1, Njet \right) \quad (4.18)$$

and

$$\vec{V}_c = \left( \frac{\partial \Delta F_c^2}{\partial X_i^j} \sqrt{\sigma_i^j}, \dots, \quad i = 1, 4 \text{ and } j = 1, Njet \right) \quad (4.19)$$

If in addition to the 4 energy and momentum conservation constraints we impose  $N$  others constraints, then we have a system of  $4 + N$  linear equations with  $4 + N$  unknowns that are the Lagrange multipliers  $\lambda_c$  and  $\lambda_{(\alpha,\beta)}$ . The system is solved iteratively :

1. We calculate  $\Delta M_{(\alpha,\beta)}^2$  and  $\Delta F_c^2$  using the initial measured set of variables  $X_i^{j0}$  and then solve the equation by a simple matrix inversion to get the Lagrange multipliers.
2. Use the obtained Lagrange multiplier in equation 4.10 to get the new set  $X_i^j$ .
3. Repeat the iteration till convergence.

### 4.3.2 Convergence

The iterations are stopped and the process is considered to be convergent when all the following conditions are satisfied simultaneously:

1.  $|\Delta F_c^2| \leq 0.01 GeV^2$  for  $c = 1$  to 4
2.  $|\Delta M_{(\alpha,\beta)}^2| \leq \frac{\Gamma_{(\alpha,\beta)}^2}{4}$  for all the constraints  $(\alpha, \beta)$ . The parameter  $\Gamma_{(\alpha,\beta)}$  is the width of the particle  $M_{\alpha,\beta}^{th}$  in the case of invariant mass constraint or any other arbitrary small number.

If the number of iterations exceeds 10 before convergence is reached then the process is considered to diverge.

### 4.3.3 Derivatives

The derivatives involved in the linear system of equations can be obtained easily given that the analytical form of the constraint is known. In the case of energy momentum conservation and invariant masses constraints on pair of jets we have:

$$M_{(\alpha,\beta)}^2 = \sum_{m=1}^4 (X_m^\alpha + X_m^\beta)^2 \epsilon_m \quad \epsilon_m = 1 \text{ for } m = 4 \text{ and } = -1 \text{ otherwise} \quad (4.20)$$

$$\implies \frac{\partial \Delta M_{(\alpha,\beta)}^2}{\partial X_i^j} = 2(X_i^\alpha + X_i^\beta)(\delta_{(\alpha,j)} + \delta_{(\beta,j)})\epsilon_i \quad (4.21)$$

and

$$F_c^2 = \sum_{\ell=1}^4 (X_c^\ell)^2 \quad (4.22)$$

$$\implies \frac{\partial \Delta F_c^2}{\partial X_i^j} = 2X_i^j \delta_{(i,c)} \quad (4.23)$$

One can see that most of the derivatives are equal to zero.

### 4.3.4 $\chi^2$ probability

At the end of the iterative process a  $\chi^2$  probability can be calculated using simply the expression of  $\chi_0^2$  and the values  $X_i^j$  found at the end of the process, with the number of constraints equals to 4 plus the number of additional constraints. However, the meaning of this probability depends highly on the weights  $w_i = \frac{1}{\sigma_i^2}$  associated to the variables  $X_i^j$  during the minimisation process.

### 4.3.5 Weights estimate

Here the weights are simply the resolution of the jet parameters (i.e. resolution of  $E$  and  $\vec{p}$ ) defined in section 4.1.1. Classically it is assumed that the errors follow normal distributions and therefore, in the case this condition is not satisfied the PULLS are studied in the iterative process and corrections are applied to the initially defined errors to make the PULLS following the  $N(0,1)$  distribution.

Since our goal is to optimise the discrimination of  $W^-W^+$  events from signal events we have chosen to study the weights, as a function of a set of constructed variables having an obvious strong influence on the resolution of the jet measured quantities:

- **Energy sharing between jets**

When two initial partons are emitted from the interaction vertex in almost the same direction, the resulting hadron showers often overlap. This can introduce a significant bias in the energy assignment to the jets at the detector level, mainly when the energies of the two initial partons are very different. This effect can be evaluated by the study of the resolution as a function of the variable:

$$\alpha_{energy\ sharing} = \frac{E_{closest\ jet}}{E_{jet}} \quad (4.24)$$

Where  $E_{jet}$  is the energy of the jet under study and  $E_{closest\ jet}$  is the energy of the closest jet in angle.  $\alpha_{energy\ sharing}$  gets large values if the jet is a small energy jet and it is resolved close to another jet with much higher energy.

- **Colour screening**

While the effect described by  $\alpha_{energy\ sharing}$  occurs at detector level and it is jet finder dependent, a similar effect occurs at parton level before the hadronisation process. This is the QCD inter-parton coherence effect or colour screening effect. A colour charge of parton can be screened by the colour charge of another nearby parton. The screening influences the colour field and thus the fragmentation process, and leads to different hadron shower configurations. The influence of the effect on the measurement of the jet energy and momentum can be estimated [20] as a function of the variable:

$$\alpha_{colour\ screening} = \frac{1}{\sin\left(\frac{\alpha_{closest\ jet}}{2}\right)} \quad (4.25)$$

where  $\alpha_{closest\ jet}$  is the angle to the closest jet.  $\alpha_{colour\ screening}$  takes the value 1 when the parton-parton effect is minimal that is the case of back-to-back jets, and it decreases to zero for collinear jets.

- **Stable four jet event**

An effect that could affect globally the event, is the event topology that is already described in 4.1.1.1. The variable is:

$$\alpha_{y-cut} = \frac{y_{34} - y_{45}}{E_{vis}} \quad (4.26)$$

where  $E_{vis}$  is the total visible energy of the event.  $\alpha_{y-cut}$  gets large for stable four jet events.

- **Number of charged particles**

The number of charged particles  $N_{ch}$  in a jet is also correlated to all the above variables. However the variable

$$\alpha_{ch} = N_{ch}(E) - \langle N_{ch}(E) \rangle \quad (4.27)$$

where  $\langle N_{ch}(E) \rangle$  is the average number of charged particles expected for a jet with an energy equal to E, brings some extra information on how the resolution of the jet quantities is affected by non detected particles due to their low momentum or to detector acceptance.

- **Detector acceptance**

Particles detected in the barrel part of OPAL have better energy and momentum resolution than the particles measured with the endcap parts. This is due to the fact that the active tracking volume (i.e. number of sense wires) of the central tracking detectors decreases with decreasing angle towards to beam pipe. If a jet is close to the beam pipe the probability to have a significant number of badly or unmeasured tracks is high. The effect on the resolution of the jet measured quantities is then studied as a function of the variable:

$$\alpha_{geometry} = \frac{1}{\sin(\theta_{beam})} \quad (4.28)$$

The average jet energy resolution  $\Delta E/E$  as a function of the above variables is shown on figure 4.3. It indicates clearly that the jet energy resolution has a strong dependence on the chosen variables.

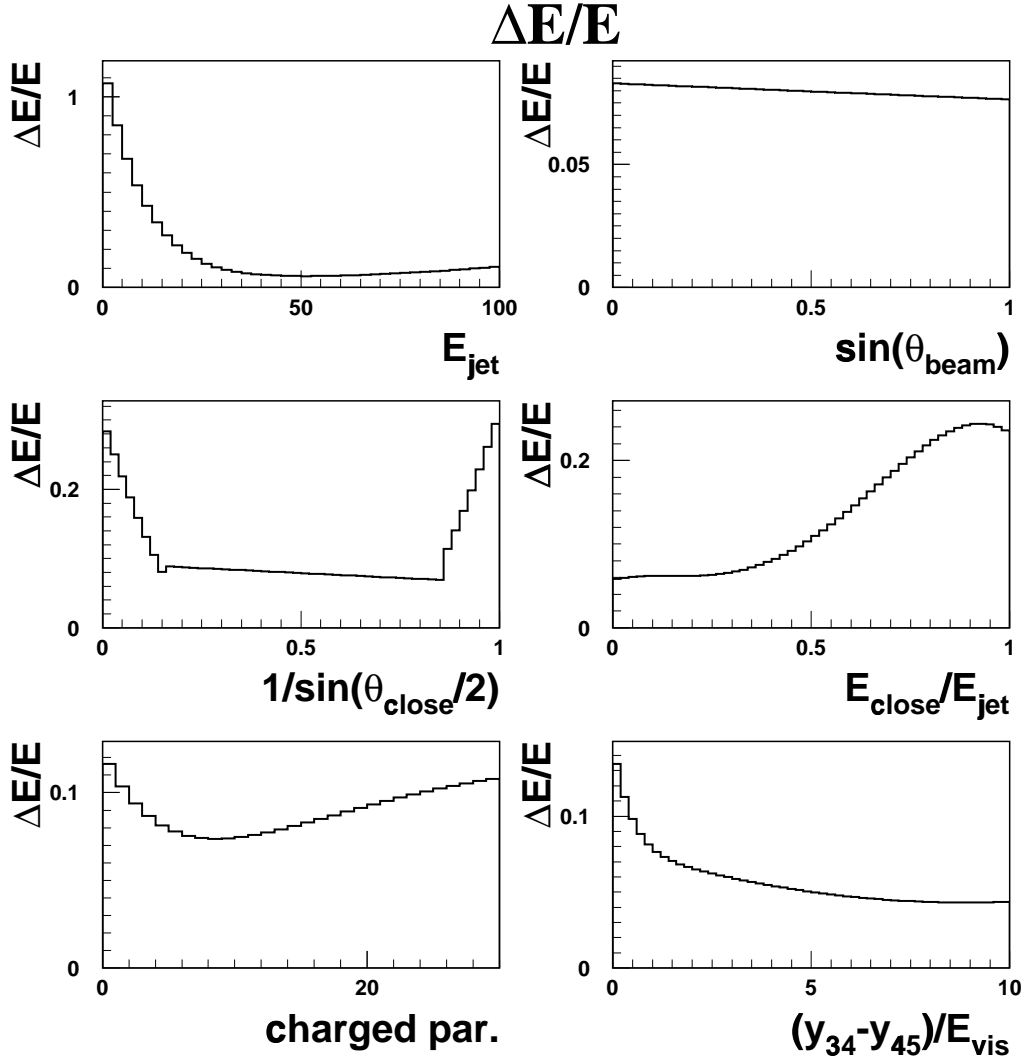


Figure 4.3:  $\Delta E/E$  versus the topology variables

#### 4.3.6 The weights parameterisation

The average resolution on the jet measured quantities (i.e. on  $E$  and  $P$ ), necessary for the kinematic fit, were measured for Monte Carlo generated events and studied as a function of the above constructed variables that are measurable at the detector level. The dependence of the average resolution on the jet measured quantities is parametrised as a function of the five above variables. This parametrisation, performed using Fourier series, would then allow an estimation of the resolution on an event by event basis for the data events. For each event the  $4 \times 4$  matrix  $\sigma_i^j$  of equation 4.7 is obtained from the Fourier coefficients of the above parametrisation.

### 4.3.7 Kinematic fit of the event

We perform on each selected 4-jet event the following test

- **$Z^0$  hypothesis:**

All the possible jet pairs (6 possible pairs) are fitted to the  $Z$  hypothesis by the minimisation of the  $\chi^2$  given in 4.7 with 5 constraints: the energy momentum conservation and one di-jet invariant mass to the  $Z^0$  boson mass. The best  $\chi^2$  probability  $P_{Z^0}$  is considered to be the probability that the event is a 4-jet event with 2 of the jets originating from a  $Z^0$  decay.

- **$W^-W^+$  hypothesis:**

All the 3 possible 2 by 2 pairing of the jets are fitted to the  $WW$  hypothesis through the minimisation of the  $\chi^2$  given in 4.7 with 6 constraints: the energy momentum conservation and the two di-jet invariant masses each constrained to  $M_W$ . The highest  $\chi^2$  probability  $P_{WW}$  is considered to be the probability that the event is a  $W^-W^+$  event.

The figure 4.4 shows the  $P_Z$  (left side) and  $P_{WW}$  (right side) obtained distributions for the three Monte Carlo event samples: the  $HZ^0$  generated events with  $M_H = 90$  GeV, the full 4 fermions  $qqqq$  sample and the two fermions  $qq$  sample. The discrimination of the  $HZ^0$  events from  $qqqq$  and  $qq$  events is clearly indicated by the  $P_Z^0$  and  $P_{W^-W^+}$  distributions. The  $HZ$  events are characterised with  $P_{Z^0} \rightarrow 1$  and  $P_{W^-W^+} \rightarrow 0$ . The two variables are combined into a single probability variable  $P_k = P_{Z^0} \times (1 - P_{W^-W^+})$ . That is the probability for an event to fit better to the  $Z^0$  hypothesis rather than the  $W^-W^+$  hypothesis.

## 4.4 The b-tagging variable $P_b$

The standard model Higgs bosons with a mass close to  $Z^0$  mass would decay preferably to a  $b\bar{b}$  pair. Therefore the identification of jets generated by  $b$  quark fragmentation would enhance the  $H \rightarrow b\bar{b}$  selection.  $B$  hadrons generated in the  $b$  quark fragmentation have longer lifetime, their hadronic decay products make a secondary vertex measurable with the OPAL tracking system (thanks to the resolution of the Silicon Microvertex detector). The semi leptonic  $B$  hadron decays are characterised with lepton that has a high transverse momentum with respect to the jet axis, and also by some other kinematic features like high particle multiplicity and a high jet mass.

The b-tagging algorithm adopted here is the standard OPAL Higgs group b-tagging algorithm described in [21] and [22]. This b-tagging algorithm identifies b-jets based on a combination of outputs from an artificial neural network and a likelihood discriminator. Here we give only a short description of the algorithm.

The b-tagging algorithm consist of two main parts: secondary vertex reconstruction and lepton tagging.

### 4.4.1 Secondary vertex

There are three different methods of identifying a secondary vertex that are used in parallel: a track-by-track method, a sub-jet method and impact parameter method. The track-by-track method consists of two algorithms: a tear-down and a build-up algorithm. The tear-down algorithm tears the event down by removing tracks one after another. Each time the removed track is the one that has the highest probability to be issued from the primary vertex, after the track is removed a new vertex reconstruction is performed. The build-up algorithm starts with the tracks that are unlikely to come from the primary vertex, and attempts to build up secondary vertices. The tear-down algorithm has a stable vertex tagging, and it is not strongly dependent on each single track used to reconstruct the secondary vertex. The build-up algorithm has a bit higher b-tagging efficiency



# Probability distributions of Z and WW

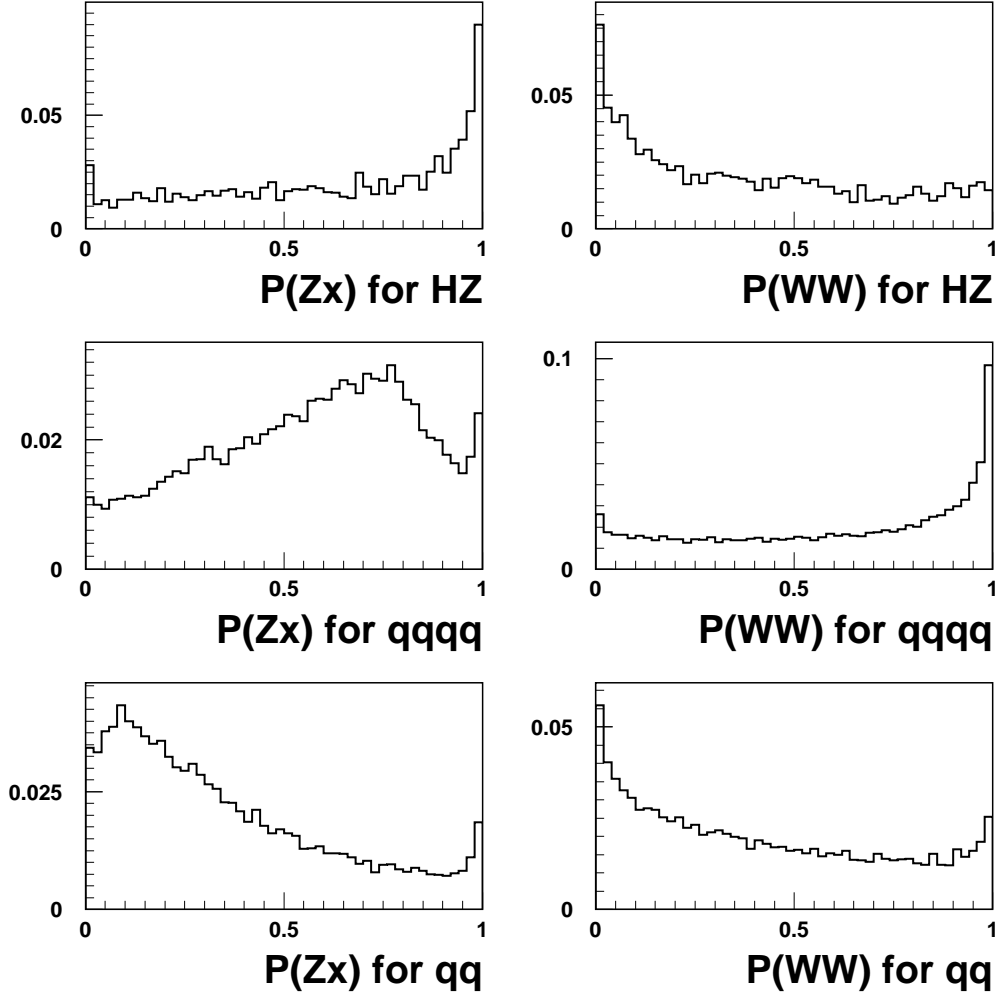


Figure 4.4: The kinematic probability distributions for Z hypothesis (5-C fit) and WW hypothesis (6-C fit) for signal and background

due to the fact that it starts with tracks that are likely to come from a hadron with longer lifetime. The two algorithm results are combined since they complementary one another.

The sub-jet method is a track-by-track algorithm as well. Each track is given a weight depending on its impact parameters, its transverse momentum with respect to the jet and its direction with respect to the beam axis. The weight associated to the track is the output of an artificial neural network (ANN). The ANN is trained such that tracks from secondary vertices get assigned larger weights. Attempt to find secondary vertices is then performed by weighted clustering of tracks into sub-jets. For each reconstructed secondary vertex the distance  $l$  to the primary and its associated error  $dl$  are evaluated.

The track measured impact parameter is used in a likelihood analysis to discriminate between decays of the different flavoured quarks.

### 4.4.2 Semi-leptonic decay

The semi-leptonic decay mode is the weak decay of the B-hadron into a charged lepton and the corresponding neutrino plus hadrons. The lepton identification is based on the recorded information from the tracking chambers, the presamplers, the electromagnetic calorimeters and the muon chambers. The information from the above detectors is combined in a likelihood analysis to provide a single probability number for each lepton candidate to be issued from a b decay.

### 4.4.3 The b-tagging probability

The above probability outputs from secondary vertex reconstruction and lepton tagging are combined, with some other kinematics related variables described in [22], are used as inputs to a last artificial neural network that provides as an output the probability that a jet is product of a b quark fragmentation.

In our case, we want 2 among the 4 jets in the event to be issued from b quarks fragmentation, this is estimated by the probability  $P_b = P_{b_i} \times P_{b_j}$ , where  $P_{b_i}$  and  $P_{b_j}$  are the final neural network outputs for the jets  $i$  and  $j$ .

Figure 4.5 shows the  $P_b$  distributions for the  $HZ^0$  with a  $M_H = 90$  GeV. signal events and for the two major background sources that are the four fermion qq $\bar{q}\bar{q}$  and the the 2 fermion qq processes. The figure indicates that  $P_b$  is a very strong discriminator between signal and background, it is a major ingredient for all the searches that contain processes involving one or more b quark jets in the final state.

## 4.5 The thrust variable $P_t$

The thrust of an event is a variable that reflects the particle or track density in each of the event hemispheres. It is defined as :

$$T = \frac{\sum_i |\vec{p}_i \cdot \hat{n}|}{\sum_i |\vec{p}_i|} \quad (4.29)$$

where  $\vec{p}_i$  is the momentum vector for each track and  $\hat{n}$  is the unit vector that maximises T. The thrust tends to 1 for events that has two back-to-back thin jets (ideally pencil-like event), and it tends towards 0 for complete isotropic events. The trust distribution is a powerful discriminator against the QCD qq like background. A probability-like variable is obtained from the parametrisation of the frequency ratio between signal and signal plus background events as a function of T.

## 4.6 The stability of the event as a 4 jet event $P_y$

The variable  $\alpha = y_{34} - y_{45}$  was already used in the weights evaluation for the kinematic fit. But we found that it adds additional power in rejecting the copiously produced 2 fermion qq events. As in the case of the thrust T distributions, the  $\log_{10}(\alpha)$  distributions are used to derive a probability like variables.

The  $\alpha = y_{34} - y_{45}$  and the thrust T distributions, normalised to surface unity, are shown on figure 4.6. A clear separation between the signal  $HZ^0$  with a  $M_H = 90$  GeV. and the QCD 2 fermion events distribution is observed.

## Probability distribution of b-tagging

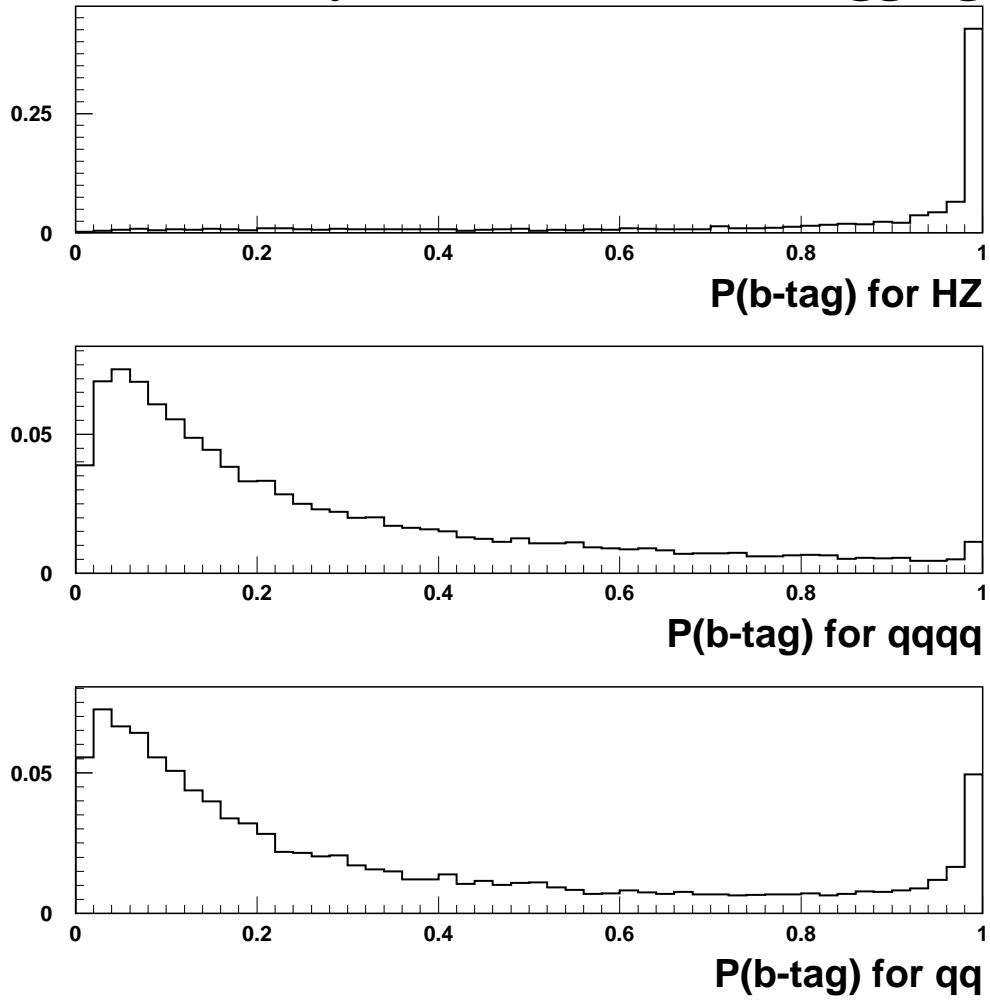


Figure 4.5: The  $P_b$  probability density function for signal  $HZ^0$  and major backgrounds  $qqqq$  and  $qq$ .

## Probability distribution of $y_{34}-y_{45}$ and Thrust

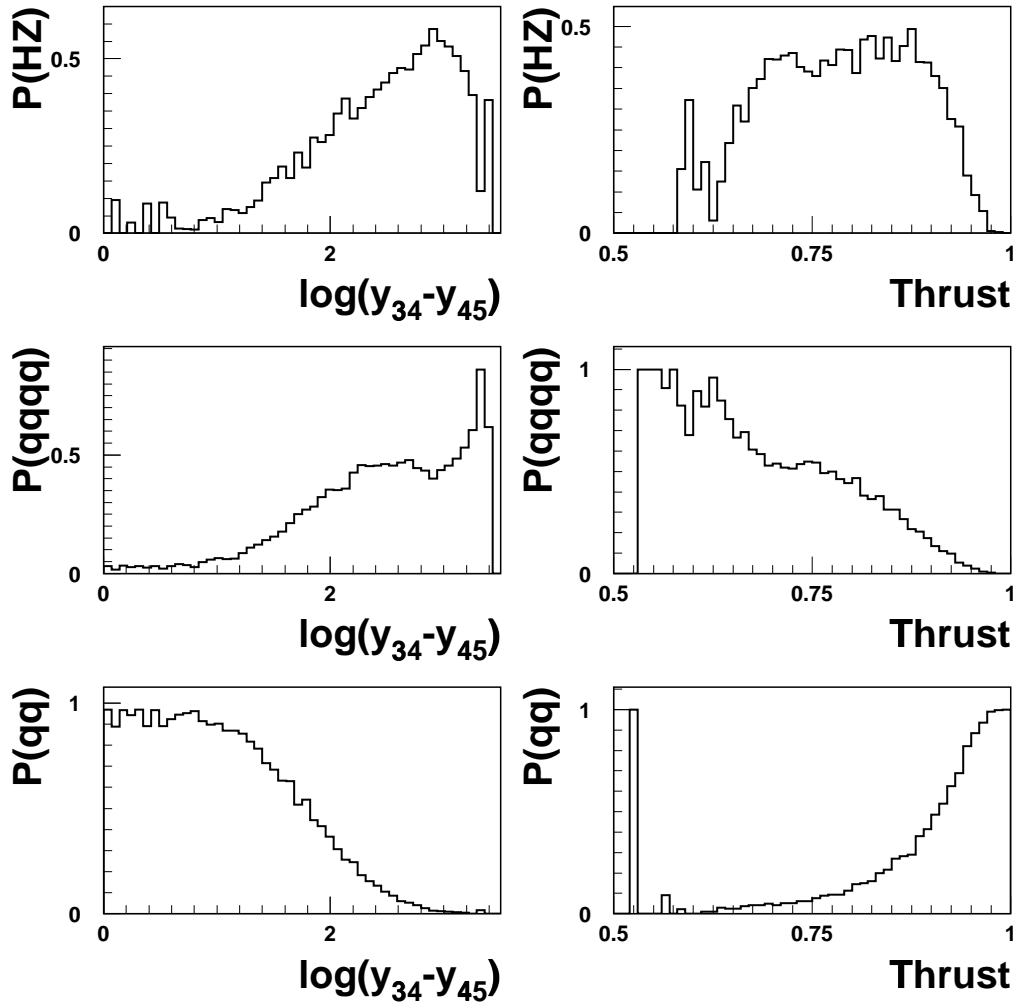


Figure 4.6: The  $\log_{10}(y_{34} - y_{45})$  and the Thrust distributions for signal and backgrounds.



# Chapter 5

## Discussion

### 5.1 The likelihood distribution

The likelihood is obtained from the four variables :  $P_k, P_b, P_t$  and  $P_y$  defined in the previous section. These variables are calculated on an event by event basis using the relation 4.6. The correlation between the variable are found to be small except for  $P_t$  and  $P_y$  that are 41% correlated. These correlations were not taken into account to derive the final result, they should be taken into account in a study of the systematic errors.

Figure 5.1 shows the likelihood distribution obtained for data as compared to the total expected background. The Standard Model expectation agrees very well with the data.

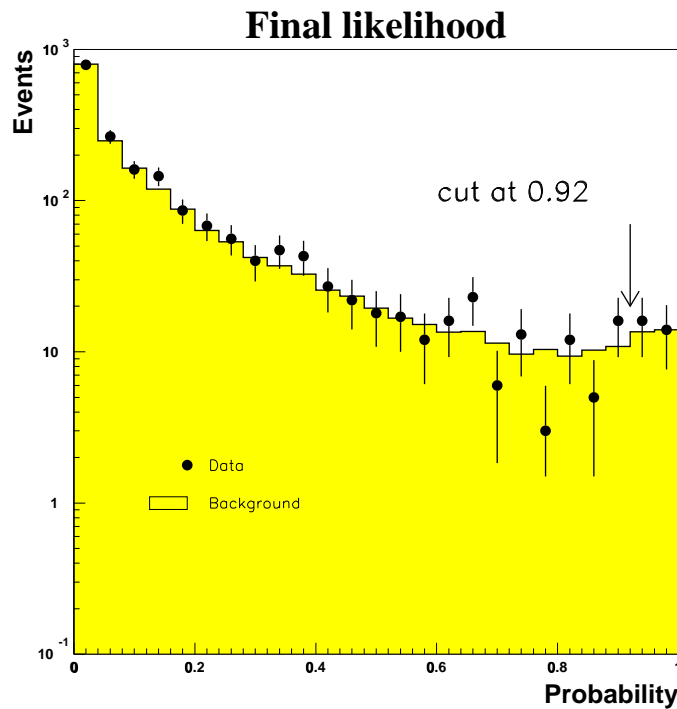


Figure 5.1: The likelihood histogram with Monte Carlo simulation of background and data from OPAL. The arrow shows where the cut in the likelihood distribution is performed.

Real data is represented by dots, the histogram filled with light grey is the expected background.

A cut in the likelihood distribution should be performed at 0.92 as explained below.

A cut on the likelihood at 0.92 leads to 30 selected events in data where the expected background is 27.4. from this and using the method described in [22]. A limit on the Higgs mass can be set at 91 GeV at the 95% confidence level.

## 5.2 Efficiency and purity

The purity and efficiency of the presented analysis depend on the number of selected events that is given by  $N_{sel} = \mathcal{L}B\sigma\epsilon$ .

The efficiency reflects how good the selection procedure is to select events while the purity is a quantity that reflects the quality of the selected event sample. Efficiency and purity are used to determine the cut in the likelihood selection. The cut is performed at the value where the product of efficiency and purity has its maximum. The purity is given by

$$Purity = \frac{\text{Number of selected and true } HZ^0 \text{ events}}{\text{Number of selected } HZ^0 \text{ and background events}} \quad (5.1)$$

The absolute efficiency is given by

$$Efficiency = \frac{\text{Number of true } HZ^0 \text{ selected events}}{\text{Number of all true } HZ^0 \text{ events}} \quad (5.2)$$

In the absolute efficiency the branching ratio for the process  $Z^0 \rightarrow q\bar{q}$  is taken into account in  $N_{sel}$  where the relative efficiency takes both the branching ratio of  $Z^0 \rightarrow q\bar{q}$  and  $H \rightarrow b\bar{b}$  into account.

The obtained efficiency and purity are shown in figure 5.2. The left figure shows likelihood versus the efficiency and purity. It can be seen that the efficiency crosses the purity at 0.92. For a likelihood cut at 0.92, we obtain 30% absolute efficiency with a purity of 31% for Higgs mass at 90 GeV. For higher Higgs masses both efficiency and purity increases.

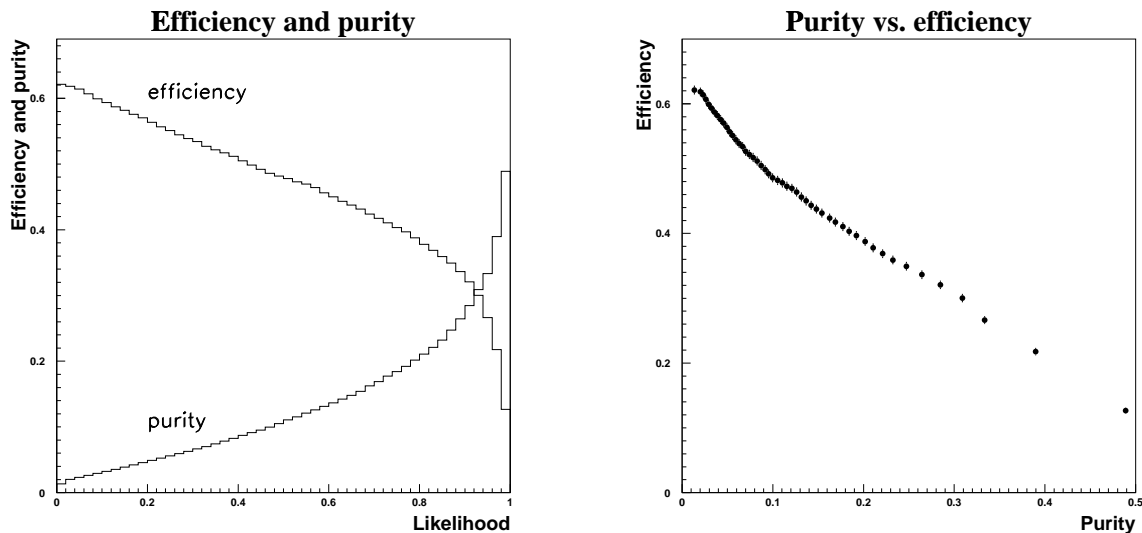


Figure 5.2: Distributions for purity and efficiency at Higgs mass = 90 GeV. Left histogram shows the efficiency and purity on top of each other versus the likelihood. The right plot shows the purity versus the efficiency.

The diagram at the right side in figure 5.2 shows the purity versus the efficiency. The error bars for the efficiency are calculated by

$$\sigma_\epsilon = \sqrt{\frac{\epsilon(1-\epsilon)}{N_{generated}}} \quad (5.3)$$

where  $N_{generated}$  is the number of generated events in the Monte Carlo simulation of  $HZ^0$  events.

### 5.3 The recoiling mass

The recoiling mass against the  $Z^0$  boson is shown in figure 5.3, where data, background and signal are normalised to surface unit. The data and the background again agree very well. If a signal

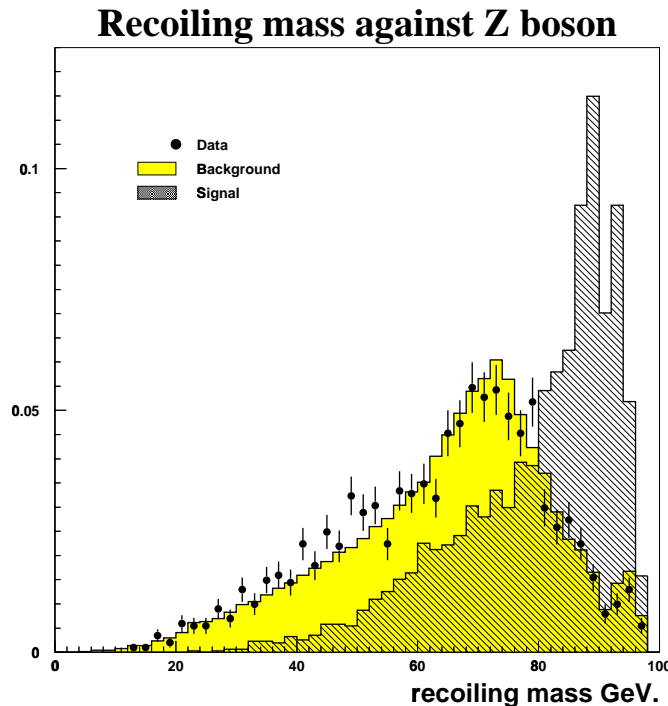


Figure 5.3: The recoiling mass against the  $Z^0$ , data, background and signal are normalised to surface unity. The signal is with generated  $M_H = 90$  GeV.

could be seen it would appear as an excess in the high mass range. The plot shows the sensitivity of the analysis to the Standard Model Higgs with a mass of 90 GeV.

With increasing number of likelihood variables the understanding of the correlations between them gets more and more difficult as well as the investigation of the systematic errors. Therefore one aim in this analysis was to use as few variables as possible. It should be mentioned though, that these input variables to the likelihood are depending on several others.

The described method is sensitive for a Higgs boson search. A study of systematic errors should to take into account mainly the correlations between the likelihood terms. This is still to be performed.





# Appendix A

## Additional plots

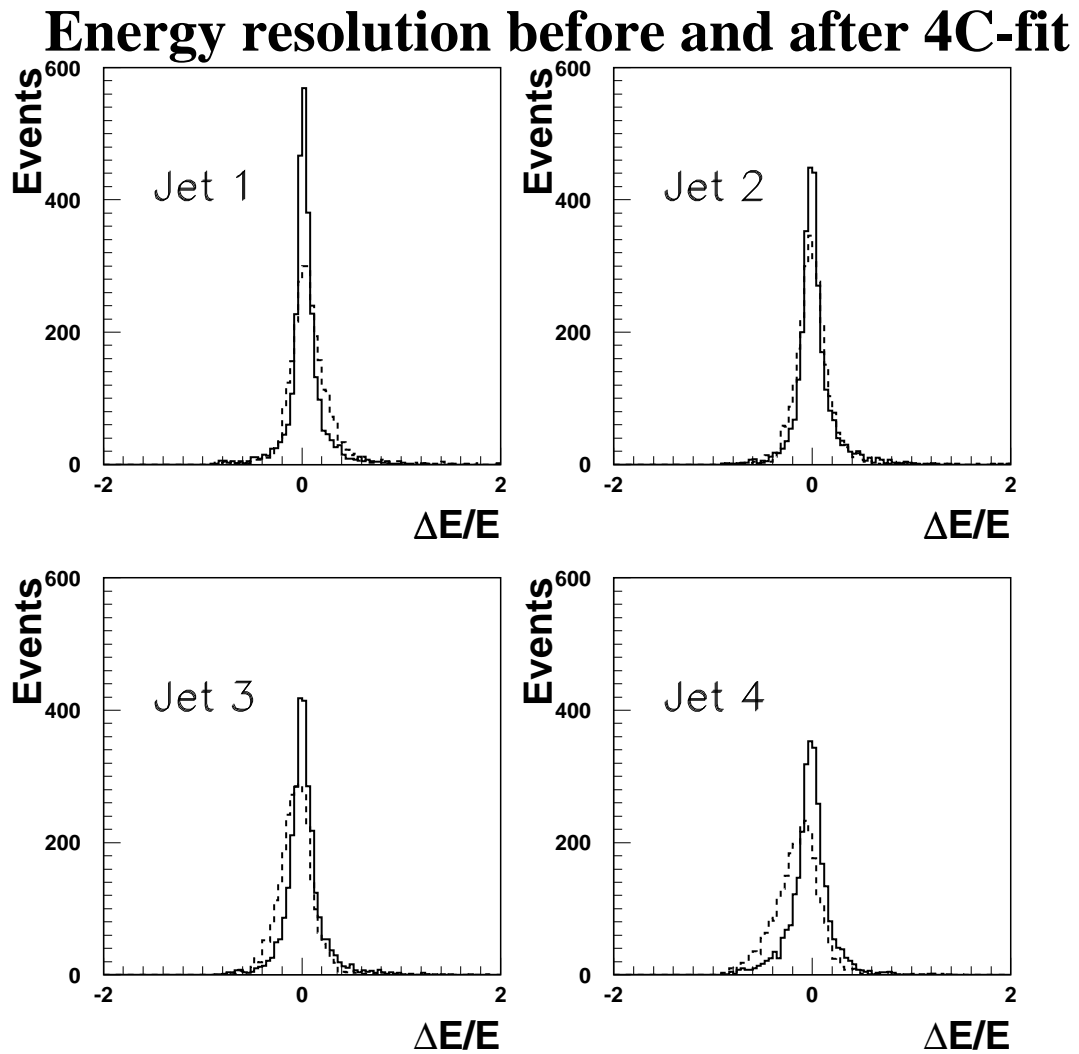


Figure A.1: The energy resolution with  $H=95$  GeV. The jets are energy ordered with Jet 1 having the highest energy.

## Angular resolution

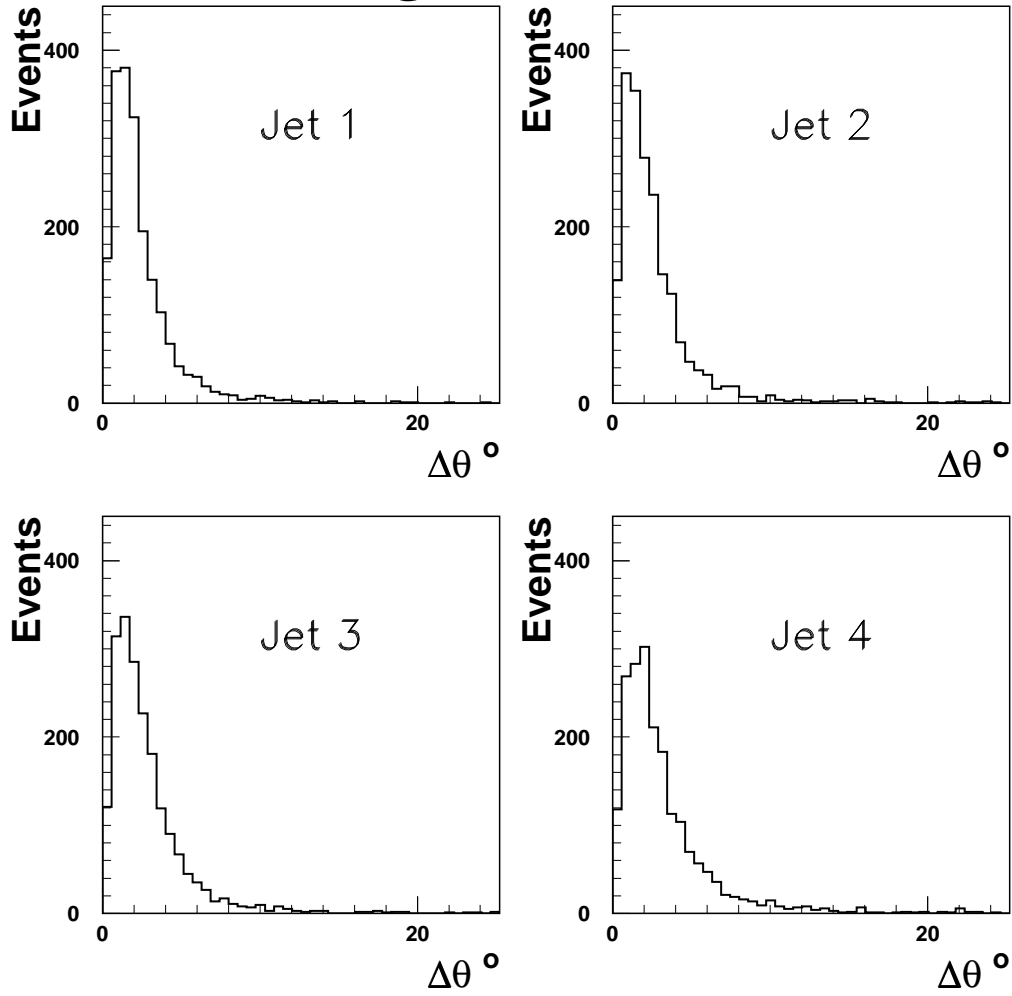


Figure A.2: The angular resolution. The jets are energy ordered with jet 1 having the highest energy. The Higgs mass =95 GeV

## Probability distributions of Z and WW

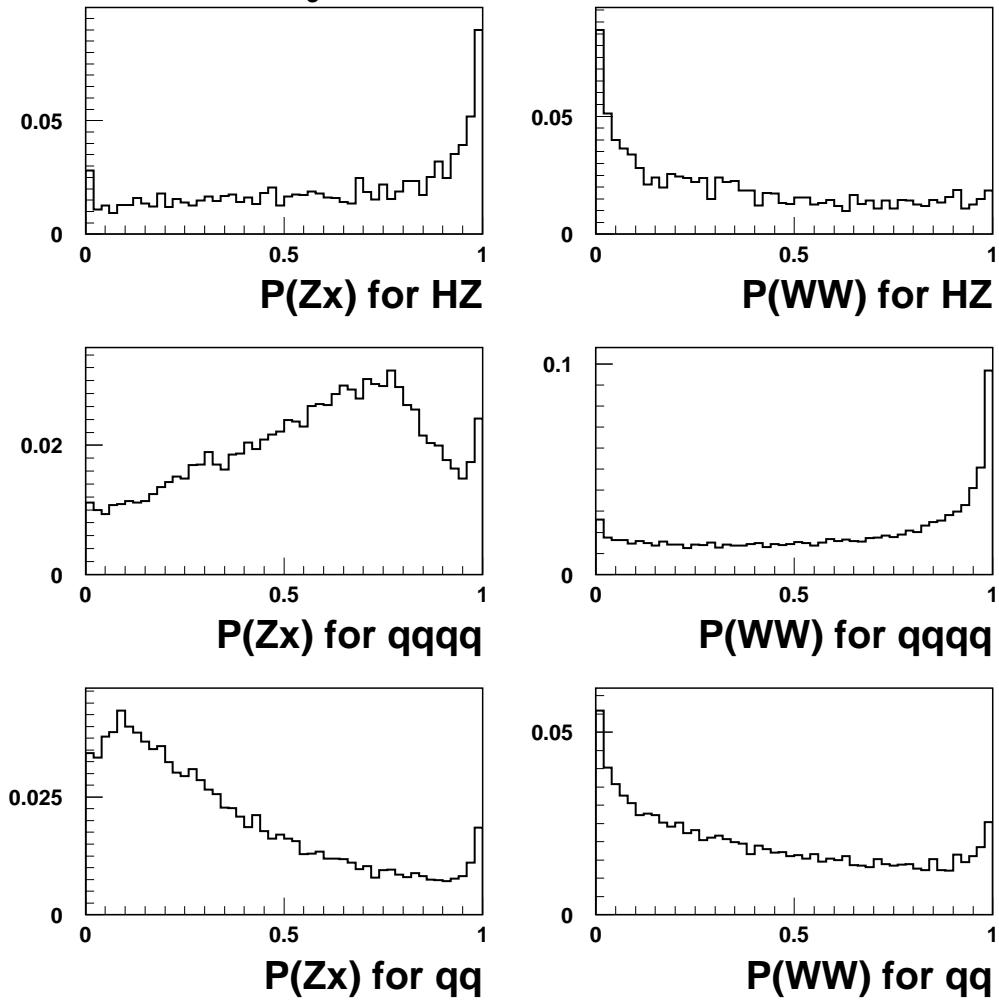


Figure A.3: The  $P_k$  variables histograms with a Higgs mass =95 GeV

## Probability distribution of $y_{34}-y_{45}$ and Thrust

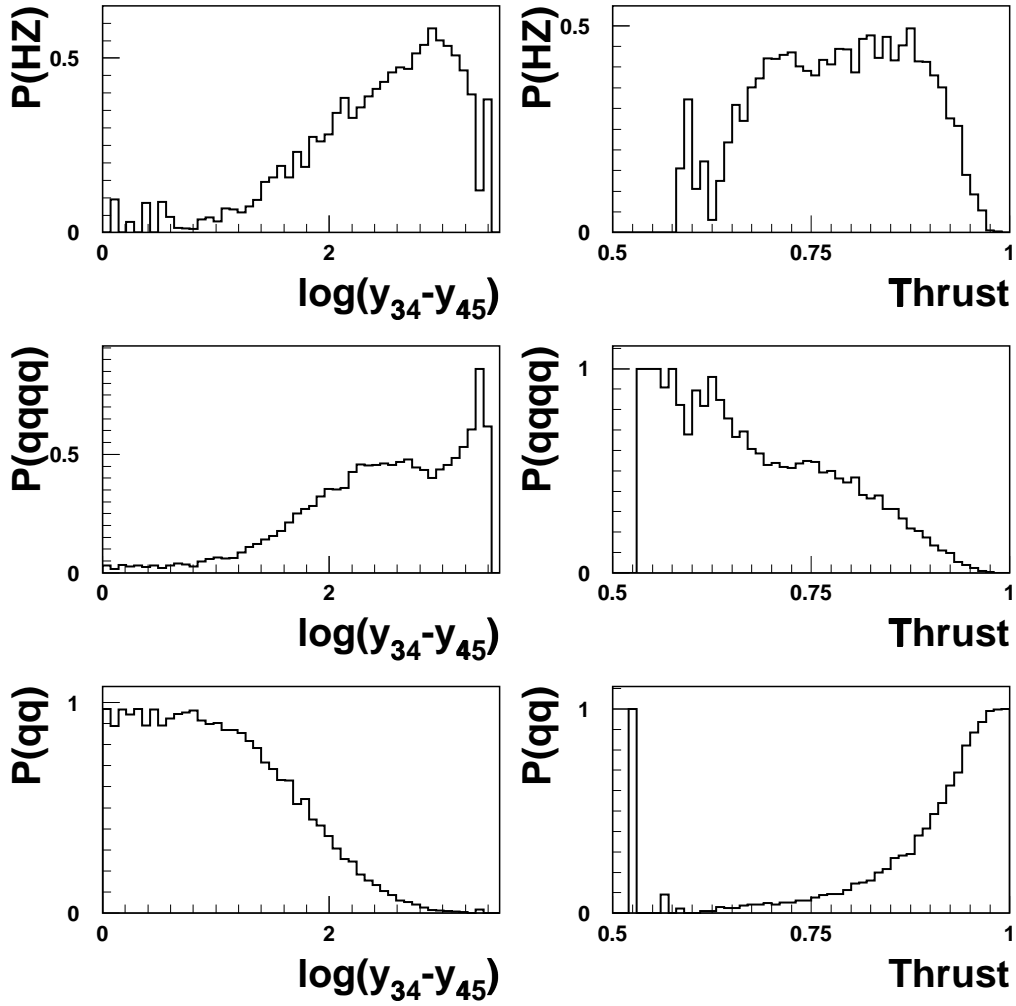


Figure A.4: The  $P_t$  and  $P_y$  variables histograms with a Higgs mass =95 GeV

## Probability distribution of b-tagging

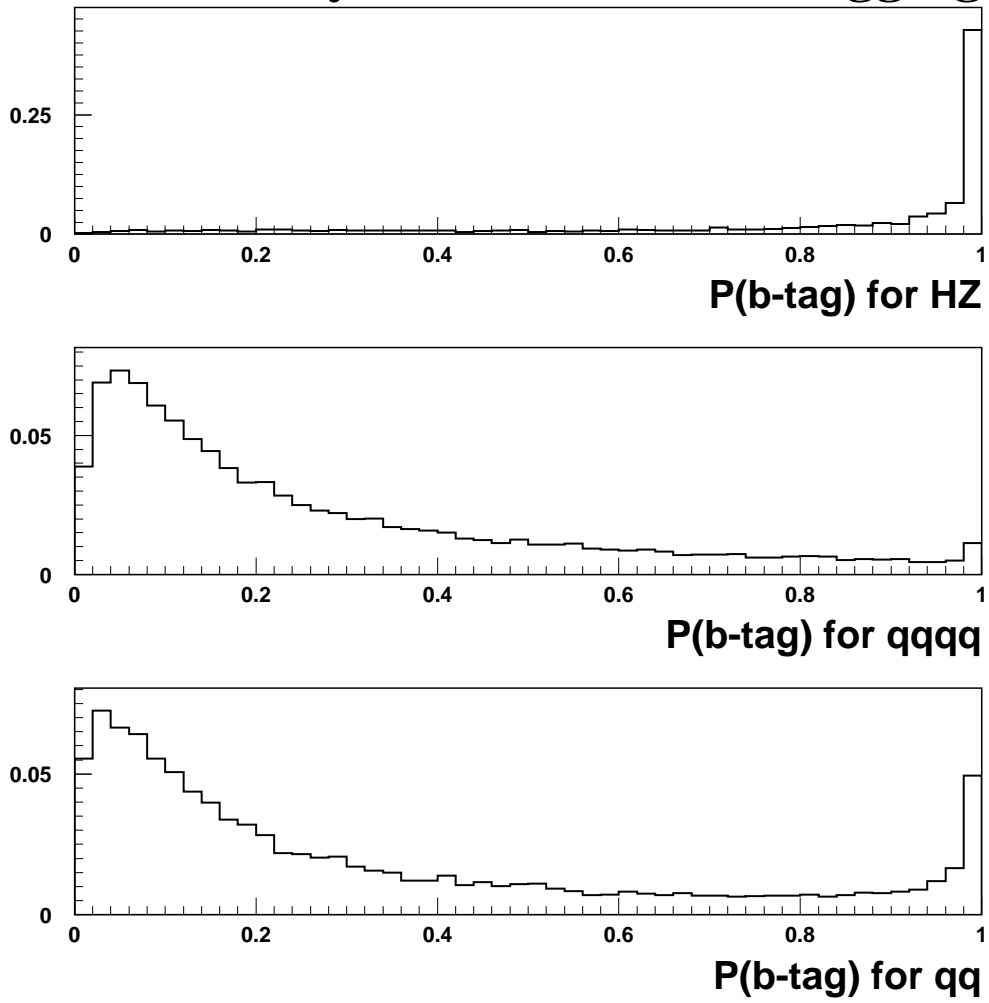


Figure A.5: The  $P_b$  variable histograms with a Higgs mass =95 GeV

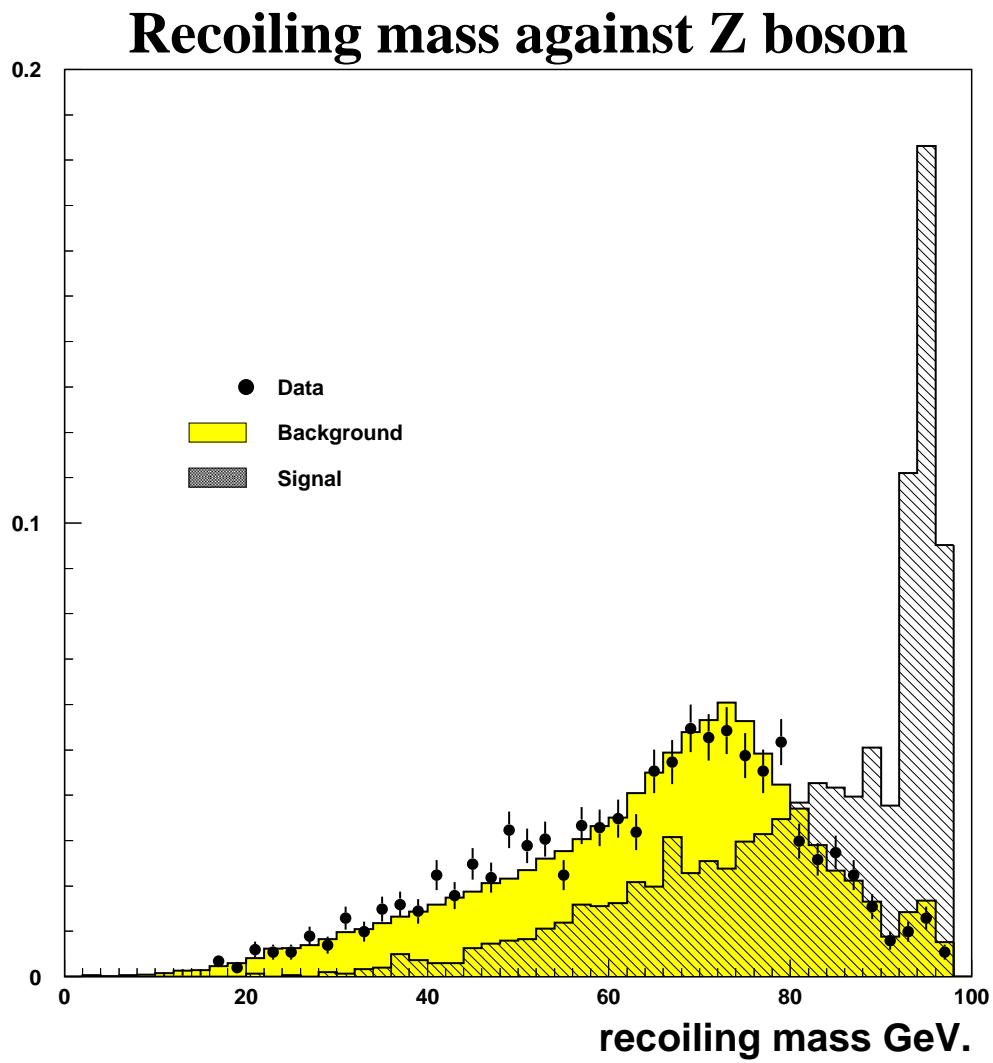


Figure A.6: The recoiling mass against the  $Z^0$  boson with a Higgs mass =95 GeV

# Bibliography

- [1] L3 ALEPH, DELPHI and OPAL Collaborations. *Limits on Higgs boson masses from combining the data of the four LEP experiments at  $\sqrt{s} \leq 183$ . CERN-EP, 99-060, 1999.*
- [2] K.Ahmet et al. OPAL Collab. *The OPAL Detector at LEP. CERN-PPE, (90-114), 1990.*
- [3] S. Anderson et al. *The extended OPAL silicon strip microvertex detector. PPE 97-092, CERN, 1997.*
- [4] W.Blum & L.Rolandi. *Particle Detection with drift Chambers.* Springer Verlag, 1993.
- [5] The European Physical Journal. *Review of Particel Physics C.* Springer Verlag, 1998.
- [6] Privat communication with Madjid Boutemour.
- [7] Thomas Cantzon Paul. *A Measurement of Tau Lepton Polarization Using the L3 Detector at LEP.* PhD thesis, The Johns Hopkins University, 1994.
- [8] Stephen G. Gasiorowicz. *Quantum physics.* John Wiley and sons, Inc, 2nd edition, 1995.
- [9] Nina Madsen. *Beauty Hadrons Lifetimes.* Master's thesis, Københavns Universitet, 1995.
- [10] Francis Halzen & Alan D. Martin. *Quarks and leptons.* John Wiley and sons, Inc., 1984.
- [11] John F. Guion et al. *Higgs Hunters Guide.* Addison-Wesley Publishing Company, 1990.
- [12] M.Veltman. *Reflections on the Higgs system.* Number 97-05. CERN report, 1997.
- [13] Chris Quigg. *Electroweak symmetry breaking and the Higgs sector. FERMILAB-CONF, (99/033-T), 1999.*
- [14] G.Abbiendi et al. OPAL Collab. *Search for Higgs Boson in  $e^+e^-$  Collisions at  $\sqrt{s} = 183$  GeV. CERN-EP, (98-173), 1998.*
- [15] K.Ahmet et al. OPAL Collab. *Lower bound for the Standard Model Higgs boson mass from the result of the four LEP experiments. CERN-EP, (98-046), 1998.*
- [16] J. Tran Thanh Van, editor. *'97 QCD & HIGH ENERGY HADRONIC INTERACTIONS.* Editions Frontiers, 1997.
- [17] Privat communication with Chris Quigg.
- [18] T. Sjöstran. Computer physics commun. **82**, 1994.
- [19] M.Olsson G.turnok & B.R.Webber S.Cantani, Yu.L.Dokshitzer. *Phys. Lett. B* 269(432), 1991.
- [20] The OPAL collaboration.  *$\pi^0, \eta$  and charged particle multiplicities in quark and . PN407, 1999.*



- [21] Satoru Yamashita and Isamu Nakamura. *LB160: Upgraded B-tagging for LEP 2*. OPAL Technical note TN 578, CERN, 1998.
- [22] The OPAL Collaboration. *Search for Neutral Higgs Boson in  $e^+e^-$  Collision at  $\sqrt{s} \approx 189$  GeV*. Submitted to European Physical Journal C, (CERN-EP/99-096), 1999.

# List of Figures

2.1	The OPAL detector. . . . .	6
2.2	Cross-section of the OPAL detector. a: perpendicular to the beam pipe and b: parallel to the beam pipe. . . . .	7
2.3	Particle identification by $\frac{dE}{dx}$ . . . . .	10
3.1	The Higgs mass versus the branching ratios [17]. . . . .	18
3.2	The first order Feynman diagram . . . . .	18
4.1	Distributions of the relative energy error. . . . .	21
4.2	The distributions of the error $\Delta\theta$ on the measurement of the jet directions. . . . .	23
4.3	$\Delta E/E$ versus the topology variables . . . . .	28
4.4	The kinematic probability distributions for Z hypothesis (5-C fit) and WW hypothesis (6-C fit) for signal and background . . . . .	30
4.5	The $P_b$ probability density function for signal $HZ^0$ and major backgrounds qqqq and qq. . . . .	32
4.6	The $\log_{10}(y_{34} - y_{45})$ and the Thrust distributions for signal and backgrounds. . . . .	33
5.1	The likelihood histogram with Monte Carlo simulation of background and data from OPAL. The arrow shows where the cut in the likelihood distribution is performed. . . . .	35
5.2	Distributions for purity and efficiency at Higgs mass = 90 GeV. Left histogram shows the efficiency and purity on top of each other versus the likelihood. The right plot shows the purity versus the efficiency. . . . .	36
5.3	The recoiling mass against the $Z^0$ , data, background and signal are normalised to surface unity. The signal is with generated $M_H = 90$ GeV. . . . .	37
A.1	The energy resolution with H=95 GeV. The jets are energy ordered with Jet 1 having the highest energy. . . . .	39
A.2	The angular resolution. The jets are energy ordered with jet 1 having the highest energy. The Higgs mass =95 GeV . . . . .	40
A.3	The $P_k$ variables histograms with a Higgs mass =95 GeV . . . . .	41
A.4	The $P_t$ and $P_y$ variables histograms with a Higgs mass =95 GeV . . . . .	42
A.5	The $P_b$ variable histograms with a Higgs mass =95 GeV . . . . .	43
A.6	The recoiling mass against the $Z^0$ boson with a Higgs mass =95 GeV . . . . .	44



# List of Tables

2.1	Different particle signals in the detectors. . . . .	8
3.1	The fermions. . . . .	13
3.2	The electroweak bosons in the Electroweak Standard Model. . . . .	14
4.1	Energy resolution. . . . .	22
4.2	The angular resolution . . . . .	22

# Persönliche Erklärung

Hiermit versichere ich, dass ich die vorliegende Arbeit selbständig und ohne andere als die angegebenen Hilfsmittel angefertigt habe.

Geneva, 11th November 1999